JOURNAL OF QUATERNARY SCIENCE (2023) **38**(2) 258–275 ISSN 0267-8179. DOI: 10.1002/jqs.3472

JQS Journal of Quaternary Science QRA Quaternary Research Association

Large-scale mass movements recorded in the sediments of Lake Hallstatt (Austria)–evidence for recurrent natural hazards at a UNESCO World Heritage site

STEFAN LAUTERBACH,[1,2,3,4]* MICHAEL STRASSER,[4] KERSTIN KOWARIK,[5] HANS RESCHREITER,[5] GERHARD W. MANDL,[6] CHRISTOPH SPÖTL,[4] BIRGIT PLESSEN[7] and ACHIM BRAUER[7,8]

[1]Kiel University, Leibniz Laboratory for Radiometric Dating and Stable Isotope Research, Max-Eyth-Str. 11–13, 24118, Kiel, Germany
[2]Kiel University, Institute of Geosciences, Ludewig-Meyn-Str. 10–12, 24118, Kiel, Germany
[3]German Archaeological Institute, Eurasia Department and Beijing Branch Office, Im Dol 2–6, 14195, Berlin, Germany
[4]University of Innsbruck, Institute of Geology, Innrain 52f, 6020, Innsbruck, Austria
[5]Natural History Museum, Department of Prehistory, Burgring 7, 1010, Vienna, Austria
[6]Graf-Starhemberg-Gasse 26/19, 1040 Vienna, Austria (formerly at Geological Survey of Austria), Neulinggasse 38, 1030, Vienna, Austria
[7]GFZ German Research Centre for Geosciences, Section 4.3 – Climate Dynamics and Landscape Evolution, Telegrafenberg, 14473, Potsdam, Germany
[8]University of Potsdam, Institute of Geosciences, Karl-Liebknecht-Str. 24–25, 14476, Potsdam, Germany

Received 22 October 2021; Revised 2 August 2022; Accepted 3 August 2022

ABSTRACT: The Bronze to Iron Age underground salt mining complex of Hallstatt (Austria) is widely recognised for its cultural importance and wealth of archaeological artefacts. However, while the daily life in the salt mines is archaeologically well documented and environmental effects of the mining activity have been investigated recently, the impact of natural hazards on the prehistoric mining community is still poorly understood. For instance, while it is well established that the prehistoric underground mines have repeatedly been destroyed by large-scale mass movements, only little is known about the characteristics and extent of these events as well as about mass-movement recurrence during more recent times. To shed light on past mass-movement activity in the vicinity of the Hallstatt salt mines, we investigated sediment cores from adjacent Lake Hallstatt. Within the regular lake sediments we identified three large-scale event deposits, which are interpreted to originate from spontaneous or seismically induced mass movements in the mid-19th and late 9th century CE and the mid-4th century BCE. While the age of the latter event is in good agreement with the abandonment of the famous Iron Age cemetery at Hallstatt, the younger events indicate that large-scale mass movements also occurred repeatedly during the Common Era.

KEYWORDS: Archaeology; European Alps; lake sediments; mass movements; prehistoric mining

Introduction

Since the establishment of settled populations, prehistoric societies worldwide have repeatedly faced natural disasters such as earthquakes (e.g. Lin & Wang, 2017), tsunamis (e.g. Papadopoulos *et al.*, 2014), volcanic eruptions (e.g. McCoy & Heiken, 2000), droughts (e.g. Haug *et al.*, 2003) or floods (e.g. Swierczynski *et al.*, 2013a), often severely affecting these societies and sometimes even leading to their demise.

The village of Hallstatt in the Northern Calcareous Alps of Austria is one of the most important places for European prehistory. This is mainly related to the exceptional long history of local underground mining for rock salt, the extent and progressiveness of the related mining facilities and techniques, and the extraordinary wealth, variety and uniqueness of the associated artefacts. This particularly holds for the Early Iron Age, for which Hallstatt consequently became the eponym (Barth & Lobisser 2002; Kern *et al.*, 2009). Because of the relevance of the Early Iron Age Hallstatt Culture and its proto-industrial salt mining complex to European prehistory, the Hallstatt–Dachstein/Salzkammergut Cultural Landscape, one of the earliest cultural landscapes worldwide, was recognised as a UNESCO World Heritage site in 1997. However, while daily life in the Hallstatt salt mines is well documented through decades of archaeological research (Barth & Lobisser, 2002; Kern *et al.*, 2009; Kowarik, 2019; Reschreiter & Kowarik, 2019) and the effects of the mining activity on the environment and landscape have been investigated very recently (Festi *et al.*, 2021; Knierzinger *et al.*, 2021), the impact of natural hazards on the prehistoric mining community is still poorly understood. For instance, while it is well-established that the prehistoric mining facilities in Hallstatt were destroyed by large-scale mass movements around the end of the Bronze Age and during the Iron Age (Rohn *et al.*, 2005; Ehret, 2009a, b), little is known about the exact timing, characteristics and extent of these events. Furthermore, even though mass movements during the last ~350 years are documented in local chronicles (Wiro-

*Correspondence: S. Lauterbach, as above.
E-mail: slauterbach@leibniz.uni-kiel.de

bal, 1994; Urstöger, 2000), their occurrence during the earlier part of the Common Era is also poorly witnessed.

Among the different types of geological archives that can be used to investigate past human–environment interactions and natural hazard recurrence, lake sediments are particularly valuable as they allow related proxy records to be established continuously and over long time intervals in the direct vicinity of the archaeological sites (e.g. Swierczynski *et al.*, 2013a; Kremer *et al.*, 2014). However, irrespective of this potential, work on the sediment infill of Lake Hallstatt, immediately adjacent to the prehistoric salt mining district, has so far been limited to the most recent deposits. While an early study utilised short surface sediment cores to generally characterise the lake's (sub-)recent sediments (Müller *et al.*, 1981), the only recent research used short surface sediment cores in combination with high-resolution multi-beam bathymetry data and reflection seismics to investigate the spatial distribution of recent subaquatic mass-movement deposits (Strasser *et al.*, 2020). In contrast, the deeper-lying sediments, which could yield substantially longer records of catastrophic mass movements and past human–environment interactions, have not been investigated so far.

To complement the rich archaeological data from the Hallstatt salt mining district, we present here the results of two coring campaigns in Lake Hallstatt, recovering sediments down to ~15 m below the lake floor. In particular, we focus on deposits of large-scale mass movements that are intercalated within the regular lake sediments. Using radiocarbon (^{14}C) dates of terrestrial plant macro remains, we employ Bayesian age modelling to establish a chronological framework for the recovered sediments, enabling the robust dating of the identified mass-movement deposits. This, together with information about possible triggers and source areas, allows them to be placed in a context with archaeological information on disturbances of the prehistoric salt mining activity.

Study site

Lake Hallstatt is located in the southern part of the Austrian Salzkammergut region (47°35′N, 13°40′E, 508 m above sea level (a.s.l.)), ~50 km south-east of Salzburg (Fig. 1a). It occupies an over-deepened north–south stretching fjord-like valley at the northern foot of the Dachstein Massif in the Northern Calcareous Alps (van Husen, 1979; Preusser *et al.*, 2010) that was shaped by glacial erosion (van Husen, 1979, 1997). The lake is ~7.5 km long and up to 1.4 km wide (lake surface area ~8.6 km^2, lake volume ~558 × 10^6 m^3) (Beiwl & Mühlmann, 2008) and established after the retreat of the Traun Glacier from the valley, which occurred at ~17 000 cal a BP (van Husen, 1979, 1997). The lake basin can be subdivided into a smaller and shallower northern part (surface area ~2 km^2, maximum water depth ~44 m) and a larger and deeper southern part (surface area ~6.6 km^2, maximum water depth ~125 m), which are separated by a shallow sill related to the delta of the Gosaubach creek (Fig. 1b). The lake's water budget is mainly controlled by the Traun River, which enters the lake at its south-eastern end, drains it in the north and provides ~53% of the inflow (Ficker *et al.*, 2011); minor inflow comes from several smaller creeks such as Waldbach, Mühlbach, Gosaubach and Zlambach (Fig. 1b). Except for flat shores in the north and south-east, Lake Hallstatt is entirely surrounded by steep-sloped mountains with Mt Plassen (1953 m a.s.l., ~3 km west) and Mt Hoher Sarstein (1975 m a.s.l., ~3 km east) being the highest peaks in the immediate vicinity. The catchment, which extends mainly to the east along the Traun River, has a size of ~646 km^2, of which 88.5% is covered by forests and sub-natural areas and only 9.5% by agricultural areas (mainly meadows) and settlements (Beiwl & Mühlmann, 2008). Hence, the impact of land use on catchment erosion and sediment supply to the lake was most likely rather low during most of the past, although the area has been occupied by humans at least since the Neolithic (Kowarik & Reschreiter, 2009; Festi *et al.*, 2021).

Prehistoric salt mining in Hallstatt

The prehistoric salt mining district of Hallstatt is located between ~900 and ~1400 m a.s.l. in a north-west–south-east-stretching high valley at the eastern slope of Mt Plassen, ~400–900 m above the lake (Figs. 1b and 1c). Although scattered artefacts indicate that there was already a human presence around 5000 BCE (Kowarik & Reschreiter, 2009), large-scale underground salt mining started only in the 14th century BCE, i.e. during the Middle Bronze Age (Grabner *et al.*, 2021). In general, the prehistoric mining activity can be subdivided into three main phases during the Middle to Late Bronze Age, the Early Iron Age and the Late Iron Age, which were all confined to separate mining areas (Figs. 1b and 1c).

The Middle to Late Bronze Age phase was characterised by underground mines in the north-western (*Nordgruppe*) and eastern-central part (*Christian-von-Tuschwerk* mining chamber) of the high valley (Fig. 1b and 1c; Reschreiter & Kowarik, 2019). According to ^{14}C and dendrochronological dating of wooden artefacts, it started around the mid-14th century BCE and lasted until the late 11th century BCE (Felber, 1974; Rom *et al.*, 1999; Stadler, 1999; Grabner *et al.*, 2021). Remarkable remains from this phase are a well-preserved wooden staircase (Reschreiter & Barth, 2005), dated to 1143 BCE (Grabner *et al.*, 2021), and remnants of wooden constructions that were used for meat curing (Barth 2013), dated to the 14th to 12th century BCE (Rom *et al.*, 1999; Stadler, 1999; Grabner *et al.*, 2021). The abrupt termination of the Bronze Age mining phase is considered to have been caused by mass movements that were triggered by strong precipitation events and favoured by the local geological setting (see below). These mass movements partly buried the high valley and destroyed the mining facilities (Ehret, 2009a).

Following a ~200-year-long episode without evidence for underground salt mining despite human presence in the high valley (Festi *et al.*, 2021; Knierzinger *et al.*, 2021), mining activity apparently recommenced during the Early Iron Age, at the latest in the 8th century BCE (Grabner *et al.*, 2021). The mines of this phase are located in the low-lying eastern-central part of the high valley (*Ostgruppe*; Fig. 1b and 1c) that was most probably not affected by the Late Bronze Age mass movements. Associated wooden artefacts mainly date between the mid-9th and mid-4th century BCE (Felber 1974; Stadler, 1999; Barth & Lobisser, 2002). The Early Iron Age mining phase was interrupted at least twice by large-scale mass movements, occurring in 662 and 570 BCE (Grabner *et al.*, 2021). This is evidenced by deposits in prehistoric mining cavities that consist of a mixture of fine-grained clastic sediments, large boulders and organics (Barth & Lobisser, 2002), being very similar to modern mass-movement deposits in the high valley (Rohn *et al.*, 2005). At present, no underground sites in the eastern-central high valley are known for the time after 570 BCE, although palaeoenvironmental data and archaeological findings indicate a persistent strong human presence in the high valley (Festi *et al.*, 2021; Knierzinger *et al.*, 2021). Associated with the Early Iron Age mining phase is a large cemetery with >1500 graves, which was in use from the early 8th to the early 4th century BCE (Kromer, 1959; Barth & Lobisser, 2002; Kern, 2009). Its extraordinary wealth and

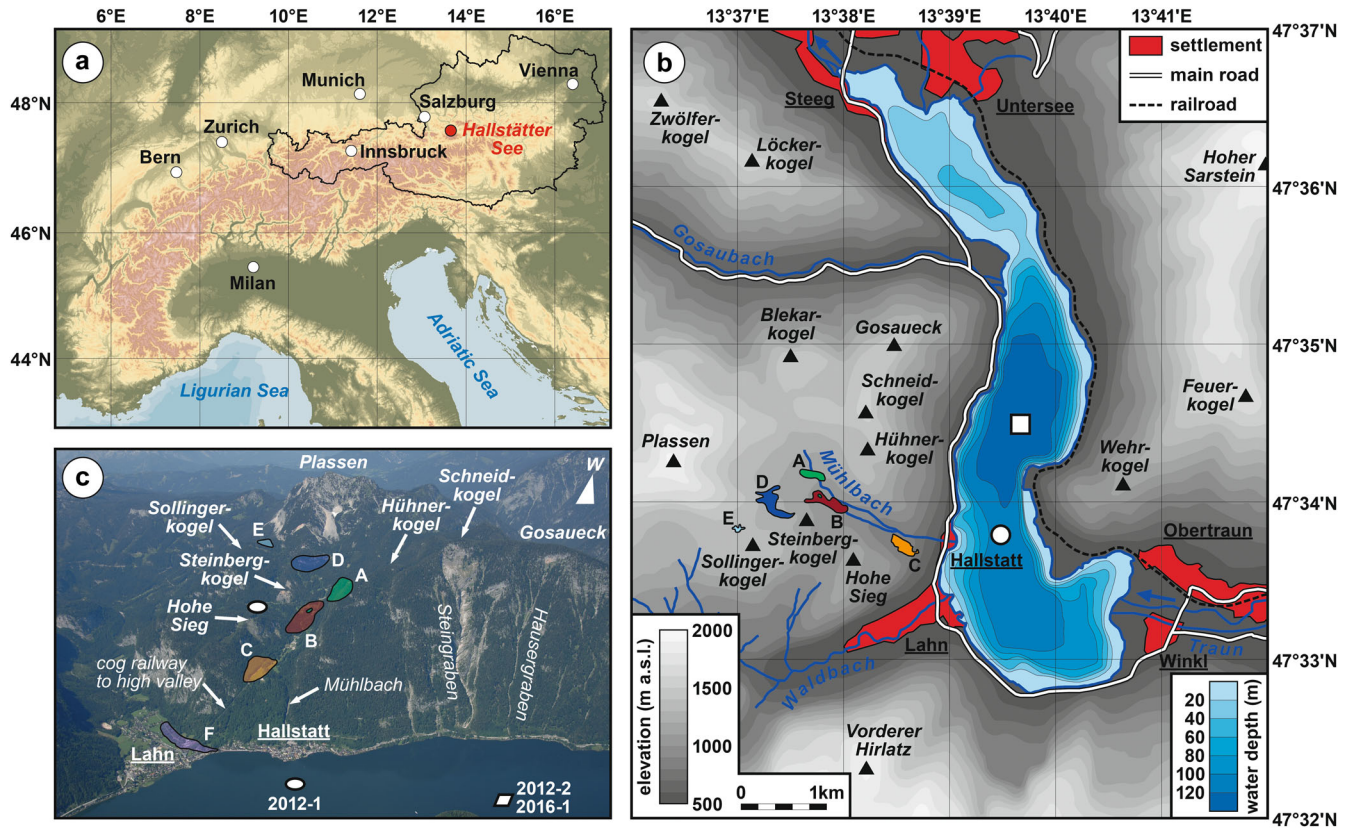

Figure 1. (a) Topographic map of the European Alps (CGIAR Consortium for Spatial Information SRTM 90 m (3 arcsec) digital elevation data (Version 4) of the NASA Shuttle Radar Topography Mission; Jarvis *et al.*, 2008) with the location of Lake Hallstatt. (b) Detailed relief map of the surroundings of Lake Hallstatt and simplified bathymetry of the lake basin (water depth in metres below lake level). Coring locations are marked by a white point (HAS_2012-1) and a white square (HAS_2012-2, HAS_2016-1) (for exact coordinates see the main text) and mountain peaks are marked by black triangles. Coloured areas indicate prehistoric mining districts and settlements (A: green – Middle to Late Bronze Age mining district (*Nordgruppe* & *Christian-von-Tuschwerk* mining chamber), B: red – Early Iron Age mining district (*Ostgruppe*), C: yellow – Early Iron Age cemetery, D: dark blue – Late Iron age mining district (*Westgruppe*), E: light blue – Late Iron Age settlement (Dammwiese wetland). (c) Aerial photograph (Aerial Photo Archive, Department of Prehistory and Historical Archaeology, University of Vienna) of the western bank of Lake Hallstatt with the villages of Hallstatt and Lahn (bold underlined) and the prehistoric salt-mining district in the high valley. Mountains peaks (bold italics) and other topographical features (italics) are given for orientation. Coloured areas indicate prehistoric mining districts and settlements as in (b) (F: purple – Roman settlement). The white point in the high valley marks the location of the Siegmoos peat bog (Festi *et al.*, 2021). Coring locations are marked by a white point (HAS_2012-1) and a white square (HAS_2012-2, HAS_2016-1). [Color figure can be viewed at wileyonlinelibrary.com]

variety of artefacts demonstrates the trans-European importance of the local salt mining complex and the associated trade and cultural exchange (Kromer, 1959; Kern, 2009). The abrupt end of human presence in the high valley after about 350 BCE, evidenced by the halt in burial activity and the reduction of human impact on the environment, is hitherto unexplained, but might also be related to mass-movement occurrence (Festi *et al.*, 2021).

The youngest prehistoric mining phase dates to the Late Iron Age. It started in the 2nd century BCE (Reschreiter & Kowarik, 2009) with mines located in the high-lying south-western part of the high valley (*Westgruppe*; Fig. 1b and 1c). Although numerous underground mines and intense human activity have previously been documented, knowledge about this mining phase is limited as the respective sites are no longer accessible (Reschreiter & Kowarik, 2009). The Late Iron Age mining phase is closely related to a settlement at the south-eastern foot of Mt Plassen (Dammwiese wetland; Fig. 1b and 1c), which has been assigned to the La Tène D period (Hell, 1952), broadly in agreement with the ^{14}C date of a wooden shovel (2050 ± 80 ^{14}C a BP; 354 BCE to 201 CE) from the *Westgruppe* mining chambers (Felber, 1974; Stadler, 1999).

In contrast to prehistoric times, traces of human activity in the high valley after the Late Iron Age are relatively scarce. Although remnants of a Roman settlement and cemetery on the south-western shore of Lake Hallstatt (Fig. 1c), as well as palaeoenvironmental data, provide evidence for a substantial human presence between the 1st and 4th century CE (Felber, 1970; Igl, 2009; Festi *et al.*, 2021), indications of associated mining activity in the high valley are scarce, except for a single ^{14}C-dated wooden artefact (1850 ± 80 ^{14}C a BP; 25 BCE to 401 CE) from the *Westgruppe* salt mines (Stadler, 1999). Evidence for mining activity in the high valley is also lacking for the time after the Roman period until the early 14th century CE; since then the mines have been in operation until today without any noteworthy interruption (Barth & Lobisser, 2002).

Geological setting

The geology of the surroundings of Lake Hallstatt is characterised by two successions of sedimentary rocks, which were deposited between the Upper Permian and Lowermost Cretaceous and subjected to complex multi-stage deformation, thrusting and nappe stacking during the Alpine orogeny (Faupl & Wagreich, 2000; Mandl, 2000).

Evaporites of the Upper Permian Haselgebirge Formation constitute the basal part of the first succession (Schäffer, 1982; Mandl, 2000; Mandl *et al.*, 2012). This argillaceous and intensively deformed breccia-like mélange, which mainly consists of silt and mudstones, anhydrite, gypsum, and halite

(Leitner & Spötl, 2017), is exposed in the Hallstatt high valley (Schäffer, 1982; Mandl *et al.*, 2012) and has been explored for rock salt since prehistoric times (Kern *et al.*, 2009). The Haselgebirge Formation is overlain by shallow-marine calcareous silt- and sandstones of the Lower Triassic Werfen Formation (Schäffer, 1982; Mandl, 2000; Mandl *et al.*, 2012), which were covered during the Middle to Upper Triassic by shallow- and deep-marine carbonates (Gutenstein Formation, Steinalm Formation, limestones of the Hallstatt Group) that were deposited under the influence of synsedimentary diapirism of the Haselgebirge Formation evaporites. The Middle to Upper Triassic carbonates are overlain by marls and marly limestones of the Uppermost Triassic Zlambach Formation and the Lower Jurassic Allgäu Formation (Schäffer, 1982; Mandl, 2000; Mandl *et al.*, 2012).

The second succession consists of a more than 2 km thick sequence of Middle to Upper Triassic platform carbonates, including the Wetterstein Dolomite, the Hauptdolomit and limestones of the Dachstein Formation, which is the dominant geological unit around Lake Hallstatt. At the end of the Triassic, platform growth terminated and the drowning platform was covered by a condensed sequence of red crinoidal and ammonoidal limestones (Hierlatz Formation, Klaus Formation). Subsidence reached its maximum in the earliest Upper Jurassic, when radiolarites and siliceous limestones of the Ruhpolding Radiolarite Group as well as escarpment breccias were deposited (Schäffer, 1982; Mandl, 2000; Mandl *et al.*, 2012). At that time, tectonic movements led to a reconfiguration of the two sedimentary realms. In particular, the first succession, which includes the Haselgebirge Formation and the Hallstatt Group limestones, was sheared off along the evaporitic basement and placed as large sliding nappes, blocks and breccias in the radiolarite basins of the subsided Dachstein platform. This new configuration was then sealed during the Upper Jurassic to Lowermost Cretaceous by limestones of the Plassen and Oberalm Formation (Mandl, 2000; Mandl *et al.*, 2012).

In the following, large-scale deformation and thrusting affected the Northern Calcareous Alps between the Early Cretaceous and Late Eocene (Faupl & Wagreich, 2000; Mandl, 2000). As a result, the relatively rigid limestones of the Hallstatt Group and the Plassen Formation now directly rest on evaporites and marls with a ductile to plastic behaviour (Rohn *et al.*, 2005). Because of this *hard-on-soft* setting (Poisel & Preh, 2004) with contrasting petrophysical properties of the rocks, the rigid limestone slabs become easily dismembered, favouring lateral extensional movement along topographic gradients (Rohn *et al.*, 2005). This often occurs in combination with secondary mass movements such as rockfalls or the toppling of rock towers (Rohn *et al.*, 2005), which may further activate mass movements through loading of the ductile, low-permeability substratum (cf. Rohn *et al.*, 2004). For example, a rockfall in 1985 CE at the eastern edge of Mt Steinbergkogel (Fig. 1b and 1c), which resulted from the *hard-on-soft* setting, mobilised a rock volume of ~32 000 m^3 (Rohn *et al.*, 2005). Superficial leaching of the Haselgebirge Formation as well as weathering of the Triassic to Jurassic marls and Quaternary moraines provide additional material to be mobilised by mudflows.

Methods

Fieldwork and sampling

Several sediment cores were recovered from two sites in the deep southern sub-basin of Lake Hallstatt (Fig. 1b) during two coring campaigns in May 2012 and June 2016, which were carried out by the German Research Centre for Geosciences (GFZ) using a 90 mm UWITEC piston corer and a 90 mm UWITEC gravity corer with additional hammer weight. In 2012, three piston core sequences (HAS_2012_A, HAS_2012_B and HAS_2012_C; Fig. 2), each consisting of several consecutive 2 m long core segments, and one gravity core (HAS_2012_K1; Fig. 2) were recovered directly off the village of Hallstatt, distal to the subaquatic alluvial fan of the Mühlbach (site HAS_2012-1; 47°33′50″N, 13°39′23″E, ~116 m water depth; Fig. 1b). Two additional piston core sequences (HAS_2012_D and HAS_2012_E; Fig. 2), also consisting of consecutive 2 m long core segments, and another gravity core (HAS_2012_K2; Fig. 2) were obtained ~1.2 km further north in the deepest part of Lake Hallstatt (site HAS_2012-2; 47°34′28″N, 13°39′40″E, ~125 m water depth; Fig. 1b). In 2016, four additional piston core sequences (HAS_2016_A, HAS_2016_B, HAS_2016_C and HAS_2016_D; Fig. 2), also consisting of several consecutive 2 m long core segments, and three more gravity cores (HAS_2016_K1, HAS_2016_K2 and HAS_2016_K3; Fig. 2) were recovered slightly north-west of the second site from 2012 (site HAS_2016-1; 47°34′ 29″N, 13°39′36″E, ~125 m water depth; Fig. 1b).

All recovered piston and gravity cores were longitudinally split, photographed and sedimentologically described, and core segments from each site were correlated via macroscopic marker layers, resulting in three separate composite sequences. Composite sequence HAS_2012-1 is 815.5 cm long and includes two core recovery gaps, composite sequence HAS_2012-2 is 367.0 cm long and continuous, and composite sequence HAS_2016-1 is 1563.0 cm long and includes one core recovery gap (Figs 2 and 3). By correlating core segments from sites HAS_2012-1 and HAS_2016-1, a continuous master composite sequence (HAS_2012/2016) of 1279.0 cm length was constructed (Figs 2 and 4a), which was used to establish a chronology for the Lake Hallstatt sediment record (see below). Depths in the master composite sequence, HAS_2012/2016, used in this study are given as master composite depth (MCD). The upper part of the master composite sequence (above 885.0 cm MCD) is mainly composed of core segments from site HAS_2012-1 (~82%) while core segments from site HAS_2016-1 were only used to bridge two small gaps between HAS_2012-1 core segments (Fig. 2). Despite the ~15% lower sedimentation rate at site HAS_2016-1, possible effects on the master composite sequence and its chronology that could result from frequent shifts between core segments from the two sites are therefore considered negligible.

Following core splitting and correlation, one half of each core segment was stored for archive purposes and non-destructive core scanning in a cold room at the GFZ, while the second half was subsampled for (1) organic macro remains for accelerator mass spectrometry (AMS) ^{14}C dating, (2) gamma spectrometry dating, (3) geochemical analyses, and (4) prospective studies (e.g. large-scale sediment thin sections, pollen analyses, X-ray diffractometry).

Sedimentological analyses

To constrain sedimentological features visible on the core photographs, X-ray computed tomography (CT) scanning was carried out on selected core segments using a Siemens SOMATOM Definition AS medical CT scanner (voxel size of 0.2 × 0.2 × 0.3 mm^3) installed at the Medical University of

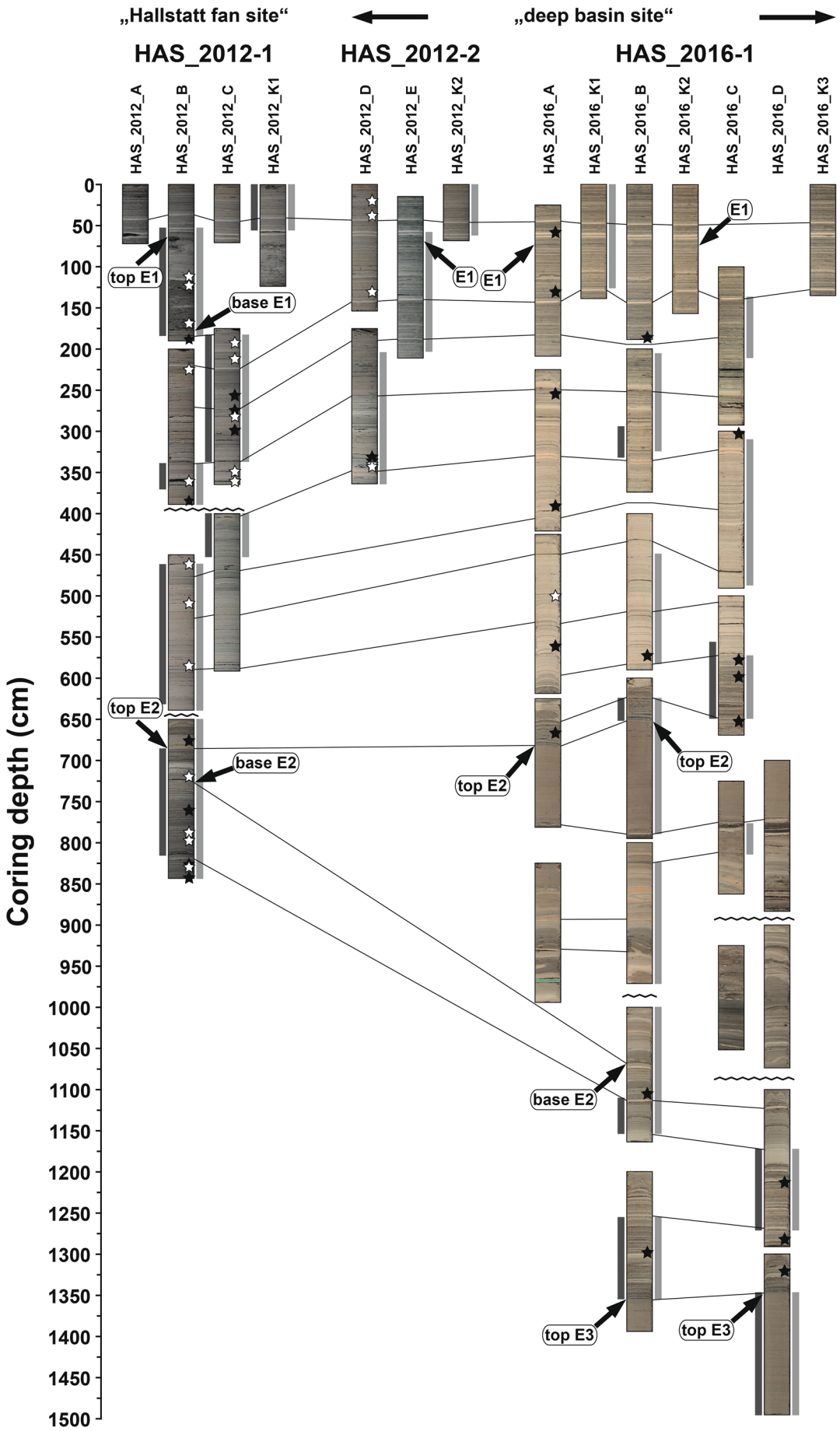

FIGURE 2 Continued.

Innsbruck. CT data visualisation was carried out using the software ImageJ.

To generally characterise different facies types of the Lake Hallstatt sediment succession, 17 representative bulk sediment samples (sediment slices 1 cm thick) were taken from the HAS_2012/2016 master composite sequence and analysed at the GFZ for their total organic carbon (TOC) content. For these analyses, ~5 mg of the homogenised sediment were placed in Ag capsules, treated with 20% HCl at 75°C, and subsequently processed in a Carlo Erba NC 2500 elemental analyser. The analytical precision of the TOC analyses is <0.1%.

Furthermore, petrographic thin sections of stones from mass-movement deposits were produced at the Geological Survey of Austria and subsequently examined under a polarisation microscope at 25–400× magnification.

Radiometric dating

To establish a chronology for the HAS_2012/2016 master composite sequence, 55 samples of terrestrial organic macro remains (deciduous tree leaves, conifer needles, wood, bark, charcoal) were collected from the obtained core segments (Figs. 2 and 3; Table 1) and AMS ^{14}C-dated at the Poznań Radiocarbon Laboratory. Conventional AMS ^{14}C dates were calibrated using the IntCal20 calibration data set (Reimer *et al.*, 2020) and the age–depth model (Fig. 4a) was established using a *P_Sequence* deposition model implemented in OxCal 4.4 (Bronk Ramsey, 2008; 2009; for further details, see the results chapter). All calibrated AMS ^{14}C ages in this study are reported as 2σ probability ranges.

Furthermore, to provide an independent age control for the most recent sediments, gamma spectrometry measurements were conducted on samples from core segment HAS_2012_D1 (Figs. 2 and 4c). Here we only report the results for the short-lived artificial radionuclide ^{137}Cs (see Strasser *et al.*, 2020). For the measurements, 1 cm thick sediment slices were taken continuously from the uppermost 38.0 cm of the core segment. After freeze-drying, 5–10 g of the sediment were put into plastic boxes and gamma counts of ^{137}Cs (661.7 keV) for each individual sample were measured by placing the sediment-filled plastic boxes into a Pb-shielded measurement chamber (located in an actively ventilated lab in the cellar of a concrete building at the GFZ) that was equipped with a CANBERRA INDUSTRIES BE 3830 broad energy germanium detector (38 cm^2 active area, 70 mm diameter, ultra-low-background cryostat). Hardware control, data storage, and spectrum analysis were realised using the Genie 2000 software (CANBERRA INDUSTRIES). Measurement times for the individual samples varied between 6 and 123 hours and the detector efficiency was determined by measuring radiocaesium-spiked milk powder (E2282, National Physical Laboratory, United Kingdom) with the same analytical setup. The overall counting uncertainty was <5%, except for two samples with <200 counts. Calculated ^{137}Cs activities are reported as mBq g^{-1}.

Results

Characterisation of the Lake Hallstatt sediments

The regular lacustrine sediments of Lake Hallstatt consist of sub-millimetre- to millimetre-scale laminated clayey-silty carbonate mud with frequently intercalated centimetre- to decimetre-scale silty-sandy turbidites (Fig. 5a and 5b). The main components of the finely laminated sediments and intercalated turbidites are endogenic calcite as well as detrital dolomite, calcite, quartz, clay minerals, micas, diatom frustules and amorphous organic matter at varying amounts in individual layers/turbidites (see Müller *et al.*, 1981). Furthermore, terrestrial macro remains such as leaves of deciduous trees (Fig. 4a), conifer needles and pieces of wood are common throughout the entire sediment sequence. Both the regular sub-millimetre- to millimetre-scale laminae and the centimetre- to decimetre-scale turbidites reveal a highly variable internal structure, colour and composition (Fig. 5a and 5b) without systematically recurring patterns, indicating a complex depositional regime. For example, different types of small-scale turbidites can be distinguished macroscopically based on their colour and grading (e.g. light yellowish grey with grading; medium to dark grey with grading; brownish grey with organic material but without grading), likely indicating different sediment sources and/or depositional mechanisms. In general, the sediment's lamination is more pronounced in the deepest part of the lake, i.e. at sites HAS_2012-2 and HAS_2016-1, than at shallower water depths, i.e. at site HAS_2012-1 (Fig. 5a and 5c). Large-scale variations in the organic matter content, reflected by changes in sediment colour, are paralleled by changes in lamination structure. For instance, distinctly laminated, dark to medium grey, relatively organic-rich sediments (1.0–2.0% TOC) prevail in the uppermost part of the sediment succession (above 323.0 cm in composite sequence HAS_2012-1; above 240.0 cm in composite sequence HAS_2012-2; above 225.0 cm in composite sequence HAS_2016-1) (Fig. 5a). In contrast, faintly laminated, yellowish grey sediments with lower amounts of organic matter (0.5–1.0% TOC) characterise the middle part of the sediment succession (between 323.0 and 621.5 cm in composite sequence HAS_2012-1 (actually, the lower boundary is slightly uncertain as it is located in a gap between two core segments); below 240.0 cm in composite sequence HAS_2012-2 (coring did not reach the lower boundary); between 225.0 and 632.0 cm in composite sequence HAS_2016-1) (Fig. 5b). The lowermost part of the sediment succession (below 621.5 cm in composite sequence HAS_2012-1; below 632.0 cm in composite sequence HAS_2016-1) is again characterised by relatively organic-rich (~3.0% TOC), distinctly laminated, dark to medium grey sediments (Figs. 2 and 5b). Outstanding features are, however, three event layers (named E1 to E3) that are intercalated in the regular lacustrine sediments and characterised by a very variable appearance and thickness in the individual core segments (Figs 2 and 5a to 5j).

The uppermost event layer, E1, is most prominent at site HAS_2012-1, directly off the village of Hallstatt, where it emerges as a 113.5 cm thick deposit (core segment

Figure 2. Overview of the sediment cores obtained from Lake Hallstatt in 2012 and 2016 and correlation between the individual core segments. Stars mark the position of AMS ^{14}C dating samples (black stars – used for the age model of the master composite sequence HAS_2012/2016, white stars – rejected). Segments of individual cores are consecutively numbered from top to bottom (e.g. HAS_2012_B1 to HAS_2012_B4). The positions of the large-scale event layers E1 to E3 are indicated. Light grey bars next to the core photographs indicate parts of the individual core segments that are incorporated in the three composite sequences HAS_2012-1, HAS_2012-2 and HAS_2016-1. Dark grey bars next to the core photographs indicate parts of the individual core segments that were used to construct the master composite sequence HAS_2012/2016. Saw-toothed lines between individual core segments indicate gaps that could not be bridged by correlation of parallel core segments. [Color figure can be viewed at wileyonlinelibrary.com]

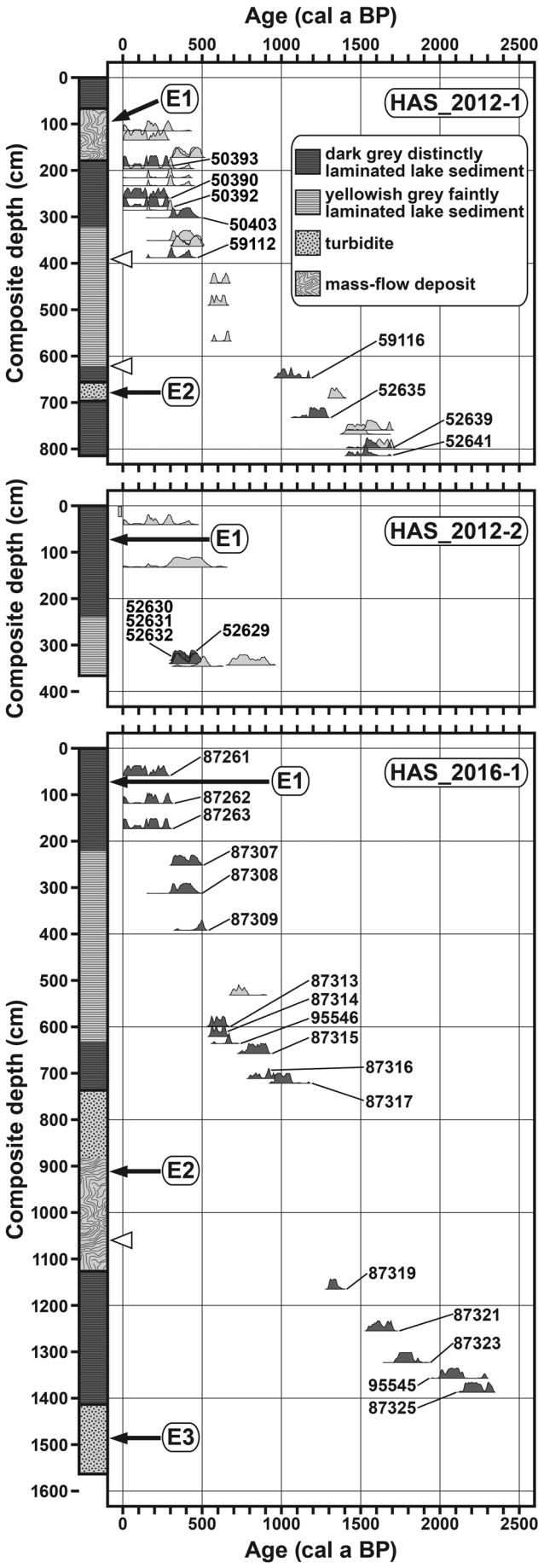

FIGURE 3 Continued.**Figure 3.** Simplified sedimentology of the three composite sequences HAS_2012-1, HAS_2012-2 and HAS_2016-1 with the positions of the obtained AMS ^{14}C dates. AMS ^{14}C dates are displayed as 2σ probability density functions (calibrated with OxCal 4.4 (Bronk Ramsey, 2009) with the IntCal20 calibration data set (Reimer *et al.*, 2020)). AMS ^{14}C dates that were used for the age model of the master composite sequence HAS_2012/2016 are displayed in dark grey with the respective sample ID (Table 1). AMS ^{14}C dates that were not included in the age model (for details see the main text) are displayed in light grey. The positions of the large-scale event layers E1 to E3 are indicated by arrows. Gaps in the three composite sequences are indicated by white triangles next to the stratigraphic columns.

HAS_2012_B1; Figs. 2 and 5c). Its basal part consists of silty-clayey carbonate mud that is mixed with poorly sorted fine sand to gravel, centimetre-scale mud clasts and large organic macro remains (e.g. pieces of wood, twigs), thus showing a matrix-supported texture (see Strasser *et al.*, 2020). This is grading into silty-clayey carbonate mud that shows diffuse and distorted light grey laminae and contains large organic macro remains. On top, a disrupted sand layer with an overlying layer of carbonate mud that partly shows intrusions of the sand layer (micro-flame structures; Fig. 5c) forms a rather sharp event-internal boundary (see Strasser *et al.*, 2020). Above this boundary, fine-grained carbonate mud with large organic macro remains and some indistinct and partly distorted millimetre- to centimetre-scale light grey laminae follows (Fig. 5c), which is overlain by a mixed layer with organic material and sand that terminates the event deposit. With respect to its spatial extent, event layer E1 at site HAS_2012-1 can be unequivocally correlated based on the characteristic pattern of the over- and underlying laminae to a ~1–2 cm thick medium grey graded turbidite in gravity cores recovered ~200 m east (Strasser *et al.*, 2020) and to a 2 cm thick medium grey graded turbidite in core segments from the deepest part of the lake basin (e.g. HAS_2016_B1; Fig. 5a). These are, however, very similar to other small-scale turbidites with respect to their composition and visual appearance (Figs. 2 and 5).

The second event layer, E2, is most prominent in the deepest part of the lake basin. While coring at site HAS_2012-2 did not go deep enough to reach this event layer, its thickness at site HAS_2016-1 is at least 390.5 cm. A more precise thickness estimate is, however, impossible because of the highly variable appearance of the basal part in the individual core segments (Fig. 2), preventing an unambiguous core-to-core correlation. At site HAS_2016-1, event layer E2 is characterised by a distinct bipartite structure. Its basal part is at least 245.0 cm thick (see above) and reveals a suite of characteristic sedimentological features, which, however, strongly vary between the individual parallel core segments, illustrating the high spatial heterogeneity of the event deposit. Although the primary millimetre- to centimetre-scale lamination of the sediment is still partly preserved, the layering is mostly distorted and disrupted and partly even tilted or folded (Fig. 5d to 5h). The boundary between the event deposit and the underlying regular lacustrine sediment is clearly visible in the CT data, showing a densified sediment-internal shear zone that separates undeformed laminated regular lake sediments from tilted and contorted event deposit sediments above (Fig. 5d). Other intervals of the basal part of event layer E2 are characterised by a rather chaotic mixture of mud clasts, sand- to gravel-sized minerogenic detritus, stones (lagoonal limestones, dolomitised limestones and coral-bearing reef-debris-type carbonates of the Dachstein Formation, micritic limestones and spiculites of the Allgäu Formation, and siliceous deepwater sediments of the Ruhpolding Radiolarite Group; Fig. 6), and larger terrestrial plant remains in a silty-clayey matrix of lacustrine carbonate mud (Fig. 5e to 5g). In addition, there are disrupted sand layers as well as liquefaction

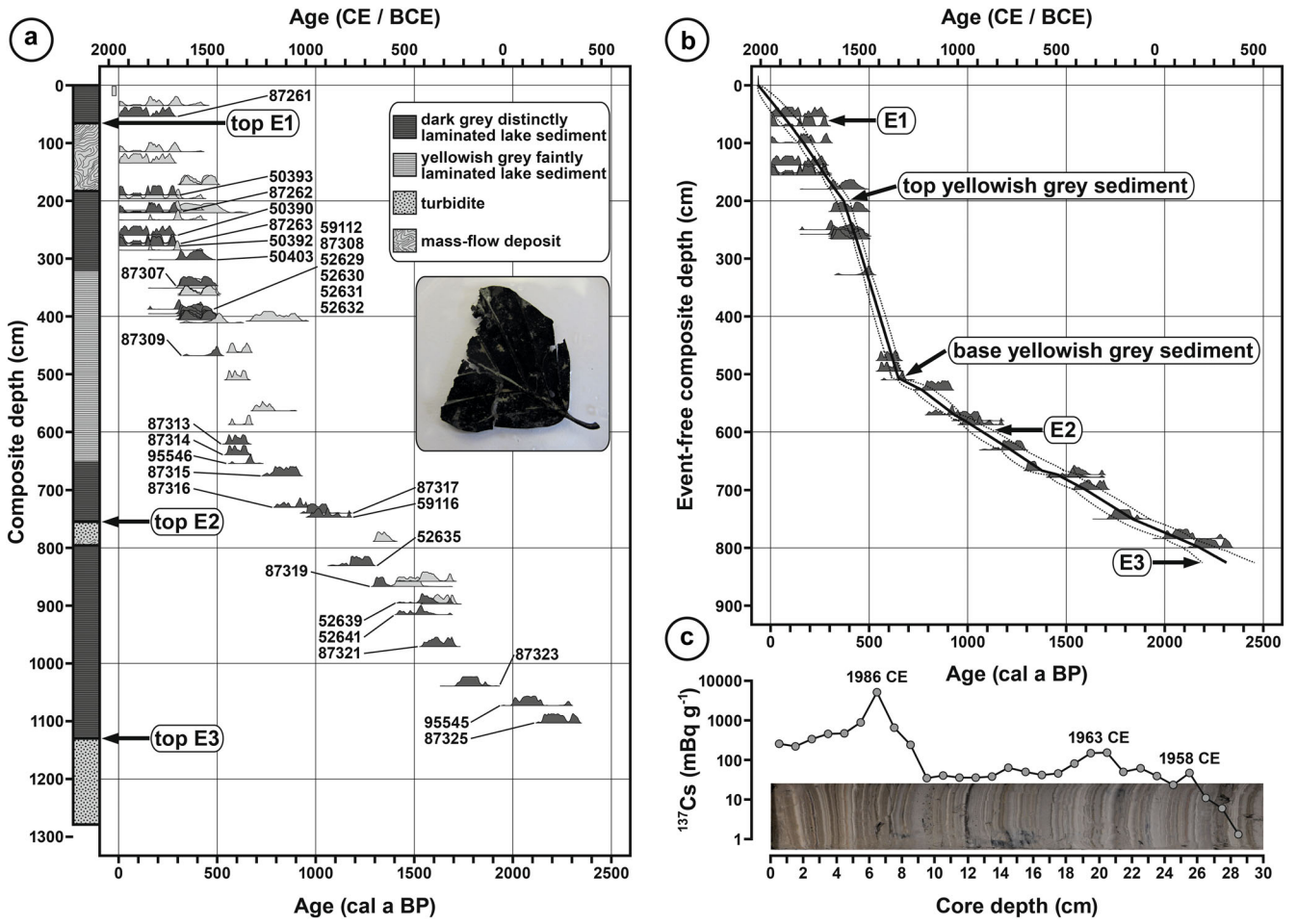

Figure 4. (a) Simplified sedimentology of the master composite sequence HAS_2012/2016 with the positions of the obtained AMS ^{14}C dates. All AMS ^{14}C dates are displayed as 2σ probability density functions (calibrated with OxCal 4.4 (Bronk Ramsey, 2009) with the IntCal20 calibration data set (Reimer *et al.*, 2020)). AMS ^{14}C dates that were used for the age model are displayed in dark grey with the respective sample ID (Table 1). AMS ^{14}C dates that were not included in the age model (for details see the main text) are displayed in light grey. The positions of the large-scale event layers E1 to E3 are indicated by arrows. The insert picture shows a typical deciduous tree leaf used for AMS ^{14}C dating (sample Poz-87314). (b) Final age model of the master composite sequence HAS_2012/2016 on the event-free depth scale (black line; dashed lines represent the 2σ uncertainty) with the positions of the AMS ^{14}C dates (displayed as 2σ probability density functions, calibrated with OxCal 4.4 (Bronk Ramsey, 2009) with the IntCal20 calibration data set (Reimer *et al.*, 2020)). (c) ^{137}Cs activity of core segment HAS_2012_D1 from the deepest part of Lake Hallstatt (site HAS_2012-2; Fig. 1b). [Color figure can be viewed at wileyonlinelibrary.com]

structures (Fig. 5d and 5e). The heterogeneous basal part of the event layer is overlain by a 145.0 cm thick turbidite that is characterised by a distinct tripartition (Fig. 5h and 5i). While the basal ~10–25 cm of the turbidite consist of multiple coarse sand layers that partly show a distinct internal grading (e.g. core segment HAS_2016_D1; Fig. 5h), its main part consists of rather homogeneous silty-clayey sediment that reveals only a slight grading (Fig. 5i). The terminal part of the turbidite is represented by a millimetre-scale clay layer, which is only visible in some core segments (e.g. HAS_2016_B4; Fig. 5i). In contrast to its prominent appearance in the deepest part of the lake basin, event layer E2 is only 40.5 cm thick at site HAS_2012-1 (core segment HAS_2012_B4; Figs. 2 and 5j). However, it reveals the same bipartite structure as at site HAS_2016-1 with (1) a ~10 cm thick basal sequence, composed of disturbed laminae with intercalated layers of mixed sandy-silty sediment, and (2) an overlying turbidite. Similar to site HAS_2016-1, the turbidite is characterised by a distinct tripartition with multiple sandy sublayers with distinct internal grading and intercalated organic-rich layers at the base, a ~16 cm thick, only slightly graded silty sublayer with some diffuse organic material above, and a ~1 cm thick clay layer at the top (Fig. 5j).

The lowermost event layer, E3, was only recovered at site HAS_2016-1 (core segments HAS_2016_B7 and HAS_2016_D4; Figs. 2 and 5k). Here, it is represented by a 149.0 cm thick, rather homogeneous sediment body of silt- to clay-sized, medium grey carbonate mud, which is interpreted as the upper part of a large-scale turbidite. However, a characteristic terminal clay layer as observed for event layer E2 could not be identified. As the coring did not go deep enough to reach the turbidite's base, its entire thickness cannot be determined and it therefore remains unknown (1) whether a sequence of distorted sediments occurs also below this turbidite and (2) how thick the complete event deposit is.

Age–depth model of the master composite sequence HAS_2012/2016 and dating of the large-scale event layers

To provide an age–depth model for the master composite sequence HAS_2012/2016 and date the three large-scale event layers, we first established an event-free depth scale (Fig. 4a and 4b). This was accomplished by subtracting all event layers (including small-scale turbidites) thicker than 2 cm from the original HAS_2012/2016 MCD scale as such layers represent

Table 1. AMS ^{14}C dates of terrestrial macrofossils from the Lake Hallstatt sediment cores. Conventional ^{14}C ages were calibrated using OxCal 4.4 (Ramsey 2009) with the IntCal20 calibration data set (Reimer *et al.*, 2020). For a detailed account on the position of the dated samples within the individual core segments, see Fig. 2. Italicised samples were not considered for the age model because of redeposited/reworked material (mostly from smaller turbidites) or very small sample size (for a detailed account, see the main text). Calibrated 2σ probability ranges of samples marked with an asterisk extend into modern times (post-1950 CE).

Sample/ lab code	Core segment	Core depth (cm)	Master composite depth (cm)	Dated material	AMS ^{14}C age (^{14}C a BP ± σ)	Calibrated age (cal a BP, 2σ)
Poz-52625	*HAS_2012_D1*	*21.00*	*18.00*	*deciduous tree leaves*	*122.41±0.37*	*-9 & -35*
*Poz-52627**	*HAS_2012_D1*	*37.00*	*35.50*	*conifer needle*	*230±50*	*0 – 441*
Poz-87261	HAS_2016_A1	33.00	54.25	deciduous tree leaves	130±30	8 – 275
*Poz-50402**	*HAS_2012_B1*	*112.00*	*115.00*	*deciduous tree leaves*	*210±40*	*0 – 421*
Poz-50404	*HAS_2012_B1*	*131.50*	*134.50*	*bark, wood*	*135±30*	*8 – 276*
Poz-50400	*HAS_2012_B1*	*169.00*	*172.00*	*bark*	*355±30*	*315 – 493*
Poz-50399	*HAS_2012_B1*	*169.00*	*172.00*	*seed (walnut)*	*375±30*	*318 – 501*
Poz-50393*	HAS_2012_B1	187.00	190.00	deciduous tree leaves	175±25	0 – 290
Poz-50398	*HAS_2012_C2*	*17.50*	*196.50*	*wood*	*260±30*	*151 – 435*
*Poz-50401**	*HAS_2012_C2*	*17.50*	*196.50*	*deciduous tree leaves*	*180±35*	*0 – 299*
*Poz-50394**	*HAS_2012_C2*	*37.00*	*216.00*	*deciduous tree leaves*	*250±30*	*0 – 429*
Poz-87262*	HAS_2016_A1	105.75	219.00	deciduous tree leaves	200±30	0 – 307
*Poz-52628**	*HAS_2012_D1*	*131.00*	*220.75*	*conifer needle*	*370±100*	*0 – 623*
Poz-50397	*HAS_2012_B2*	*25.00*	*233.00*	*deciduous tree leaves*	*260±30*	*151 – 435*
Poz-50390	HAS_2012_C2	80.50	259.50	deciduous tree leaves	135±30	8 – 276
Poz-87263*	HAS_2016_B1	187.00	274.00	deciduous tree leaves	175±30	0 – 293
Poz-50392*	HAS_2012_C2	99.00	278.00	deciduous tree leaves	180±30	0 – 295
Poz-59118	*HAS_2012_C2*	*106.50*	*285.50*	*deciduous tree leaves, conifer needles, charcoal*	*250±25*	*151 – 427*
Poz-50403	HAS_2012_C2	123.00	302.00	deciduous tree leaves	310±30	301 – 460
Poz-87307	HAS_2016_A2	29.00	347.00	deciduous tree leaves	345±30	313 – 480
Poz-50395	*HAS_2012_C2*	*173.50*	*351.00*	*bark*	*315±30*	*304 – 461*
Poz-50391	*HAS_2012_C2*	*184.00*	*361.00*	*deciduous tree leaves*	*375±35*	*316 – 504*
Poz-59111	*HAS_2012_B2*	*161.00*	*363.50*	*conifer needles*	*365±30*	*316 – 498*
Poz-59112	HAS_2012_B2	185.50	387.50	deciduous tree leaves	275±30	154 – 441
Poz-87308	HAS_2016_C2	2.50	395.50	deciduous tree leaves	315±30	304 – 461
Poz-52629	HAS_2012_D2	154.00	398.50	deciduous tree leaves	345±30	313 – 480
Poz-52630	HAS_2012_D2	160.00	405.00	deciduous tree leaves	340±30	312 – 477
Poz-52631	HAS_2012_D2	161.00	406.00	deciduous tree leaves	355±30	315 – 493
Poz-52632	HAS_2012_D2	161.00	406.00	deciduous tree leaves	365±30	316 – 498
Poz-52633	*HAS_2012_D2*	*164.00*	*408.00*	*deciduous tree leaves*	*870±70*	*680 – 915*
Poz-52634	*HAS_2012_D2*	*167.00*	*411.00*	*conifer needles*	*460±50*	*327 – 623*
Poz-59113	*HAS_2012_B3*	*10.50*	*462.50*	*deciduous tree leaves, conifer needles, wood*	*660±30*	*556 – 672*
Poz-87309	HAS_2016_A2	165.00	468.00	deciduous tree leaves	425±30	333 – 525
Poz-59114	*HAS_2012_B3*	*58.00*	*510.00*	*deciduous tree leaves, conifer needles, charcoal*	*620±25*	*552 – 651*
Poz-87310	*HAS_2016_A3*	*75.00*	*563.50*	*charcoal*	*840±30*	*684 – 788*
Poz-59115	*HAS_2012_B3*	*135.25*	*587.25*	*deciduous tree leaves*	*690±25*	*564 – 676*
Poz-87313	HAS_2016_A3	136.00	621.00	deciduous tree leaves	615±30	550 – 652
Poz-87314	HAS_2016_B3	172.50	639.50	deciduous tree leaves	625±30	551 – 656
Poz-95546	HAS_2016_C3	77.50	654.50	deciduous tree leaves	720±30	567 – 720
Poz-87315	HAS_2016_C3	99.00	676.00	deciduous tree leaves	930±30	748 – 919
Poz-87316	HAS_2016_C3	153.25	730.00	deciduous tree leaves	995±30	796 – 958
Poz-87317	HAS_2016_A4	41.50	740.00	deciduous tree leaves	1110±30	935 – 1069
Poz-59116	HAS_2012_B4	25.50	747.00	deciduous tree leaves, conifer needles, bud scales	1150±25	972 – 1177
Poz-95544	*HAS_2012_B4*	*69.00*	*789.00*	*deciduous tree leaves*	*1460±30*	*1301 – 1386*
Poz-52635	HAS_2012_B4	111.00	831.00	deciduous tree leaves	1285±35	1129 – 1291
Poz-52637	*HAS_2012_B4*	*138.00*	*858.00*	*deciduous tree leaves*	*1685±35*	*1422 – 1700*
Poz-87319	HAS_2016_B6	105.50	867.00	deciduous tree leaves	1435±30	1295 – 1371
Poz-52638	*HAS_2012_B4*	*147.00*	*867.00*	*deciduous tree leaves, wood*	*1600±35*	*1398 – 1539*
Poz-52639	HAS_2012_B4	176.00	895.50	deciduous tree leaves, conifer needles	1670±30	1420 – 1693
Poz-52640	*HAS_2012_B4*	*179.00*	*897.25*	*deciduous tree leaves, conifer needles*	*1745±30*	*1549 – 1708*
Poz-52641	HAS_2012_B4	193.00	915.50	deciduous tree leaves, conifer needles	1645±30	1413 – 1686
Poz-87321	HAS_2016_D3	114.00	971.00	deciduous tree leaves	1735±30	1547 – 1704
Poz-87323	HAS_2016_D3	184.00	1039.25	deciduous tree leaves	1880±30	1714 – 1870
Poz-95545	HAS_2016_B7	98.00	1073.00	terrestrial moss	2120±30	1998 – 2292
Poz-87325	HAS_2016_D4	21.50	1103.25	deciduous tree leaves	2230±30	2149 – 2336

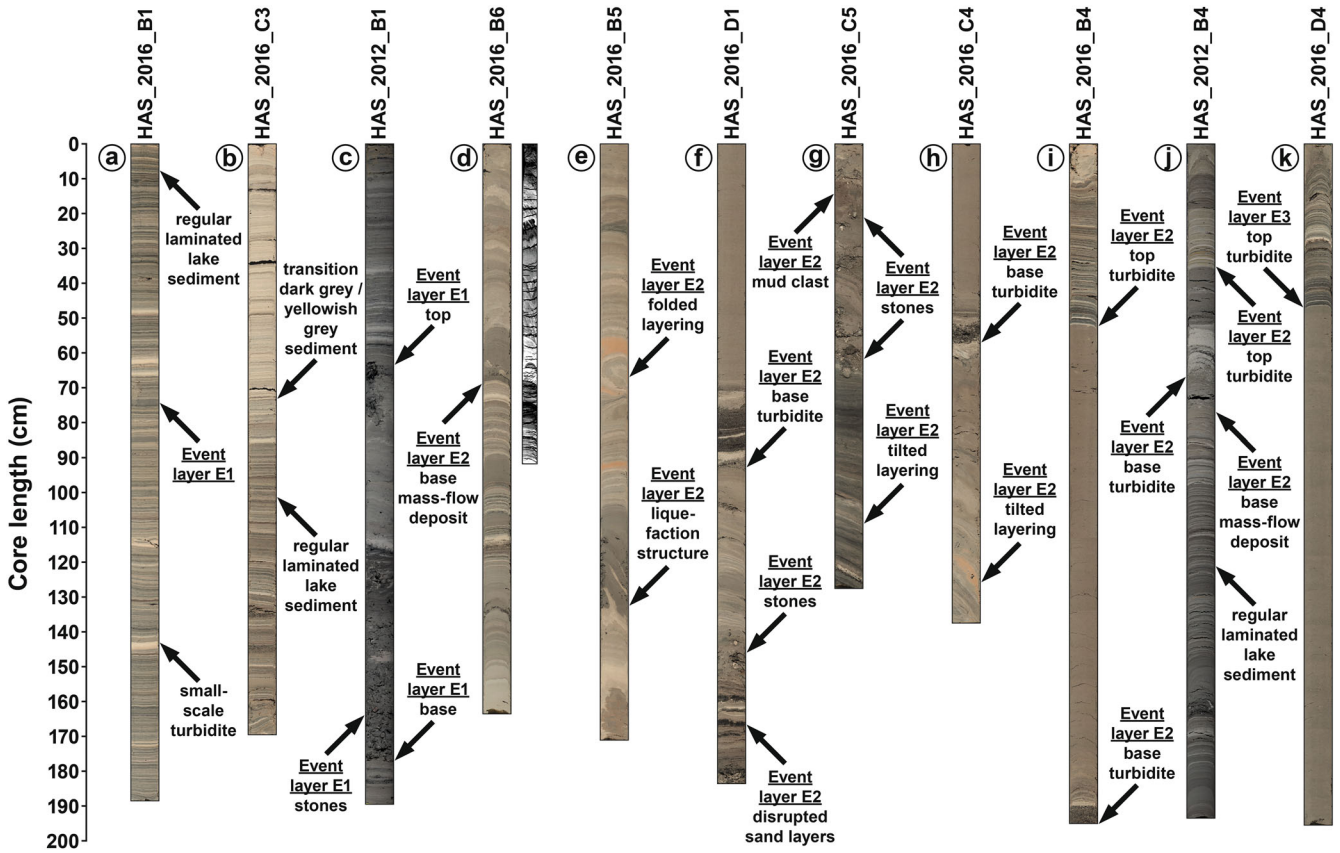

Figure 5. Photos of core segments from Lake Hallstatt, visualising characteristic features of the regular lacustrine sediments and the three large-scale event layers. The names of the individual core segments refer to their position in the respective core in Fig. 2 (e.g. HAS_2016_B1 – first (uppermost) segment of core HAS_2016_B). (a) Regular (sub-)millimetre- to centimetre-scale laminated lacustrine background sediment with some small-scale turbidites at site HAS_2016-1 (deepest part of the lake basin). The dark grey turbidite at 74.0 cm is event layer E1. (b) Transition from organic-rich, distinctly laminated sediment to carbonate-rich, faintly laminated sediments at site HAS_2016-1 (deepest part of the lake basin). (c) Event layer E1 at site HAS_2012-1 (distal to the Hallstatt subaquatic alluvial fan). (d) Base of the mass-flow deposit of event layer E2 at site HAS_2016-1 (deepest part of the lake basin). The CT scan of the core visualises the boundary between the undeformed laminated lacustrine sediments and the overlying distorted event deposit sediments at 68.0 cm. (e) Mass-flow deposit of event layer E2 with folded layering and liquefaction structures at site HAS_2016-1 (deepest part of the lake basin). (f) Mass-flow deposit of event layer E2 with disrupted sand layers and stones and the base of the overlying large-scale turbidite at site HAS_2016-1 (deepest part of the lake basin). (g) Mass-flow deposit of event layer E2 with tilted layering and stones at site HAS_2016-1 (deepest part of the lake basin). (h) Mass-flow deposit of event layer E2 with tilted layering and the base of the overlying large-scale turbidite at site HAS_2016-1 (deepest part of the lake basin). (i) Turbidite of event layer E2 with overlying regular lacustrine sediments at site HAS_2016-1 (deepest part of the lake basin). (j) Event layer E2 at site HAS_2012-1 (distal to the Hallstatt subaquatic alluvial fan). (k) Upper part of the turbidite of event layer E3 with overlying regular lacustrine sediments at site HAS_2016-1 (deepest part of the lake basin). [Color figure can be viewed at wileyonlinelibrary.com]

instantaneous depositional events. The event-free depth scale was used as the basis for the age–depth model (Fig. 4b), which was established using a *P_Sequence* deposition model implemented in OxCal 4.4 (Bronk Ramsey, 2008, 2009) with the IntCal20 calibration data set (Reimer *et al.*, 2020). The model parameter *k* was set to 1 and allowed to vary over one order of magnitude (Bronk Ramsey & Lee 2013). As input parameters we used 30 out of the 55 obtained AMS ^{14}C dates (Table 1) with their respective position on the event-free depth scale (Fig. 4a and 4b). The other 25 AMS ^{14}C dates (in italics in Table 1) were omitted from age modelling because the dated samples either (1) originated from event layers and therefore were most likely reworked, (2) consisted of material generally prone to reworking (e.g. wood, charcoal), or (3) were very small, i.e. yielded <0.5 mg of carbon. As a further input parameter for the deposition model we used the date of the first coring campaign (2012 CE) for the top of the master composite sequence (i.e. the former sediment–water interface at 0.0 cm MCD). In addition, we integrated the upper (322.5 cm MCD) and lower boundary (650.5 cm MCD) of the yellowish grey, faintly laminated middle part of the Lake Hallstatt sediment sequence (Fig. 4a and 4b) as sedimentological change points into the deposition model. The resulting age–depth model (Fig. 4b) yielded an agreement index $A_{overall}$ of 68.1%, which is above the critical threshold of 60% (Bronk Ramsey, 1995, 2008), proving the robustness of the model. Average rates of regular lacustrine background sedimentation (excluding event layers >2 cm) varied between ~4–5 mm yr^{-1} in the distinctly laminated, organic-rich sediments above 322.5 cm MCD, ~11 mm yr^{-1} in the faintly laminated, carbonate-rich sediments between 322.5 and 650.5 cm MCD, and ~2 mm yr^{-1} in the distinctly laminated, organic-rich sediments below 650.5 cm MCD.

The reliability of the AMS ^{14}C-based age–depth model in the uppermost part of the master composite sequence HAS_2012/2016 is independently confirmed by the gamma spectrometry measurements. Transferring the ^{137}Cs activity data from core segment HAS_2012_D1 via sub-centimetre-scale correlation of individual macroscopic marker layers to the master composite sequence HAS_2012/2016 allowed the identification of three chronological tie points, which are closely associated with the history of atmospheric ^{137}Cs fallout. Following the first occurrence of ^{137}Cs at 28.5 cm in core segment HAS_2012_D1 (Fig. 4c), the first ^{137}Cs activity peak (~40 mBq g^{-1}) at 25.5 cm (≙25.0 cm MCD) most likely corresponds to the first peak in atmospheric ^{137}Cs concentration that was reached in 1958 CE before the first moratorium on atmospheric nuclear weapons testing (see Appleby, 2001).

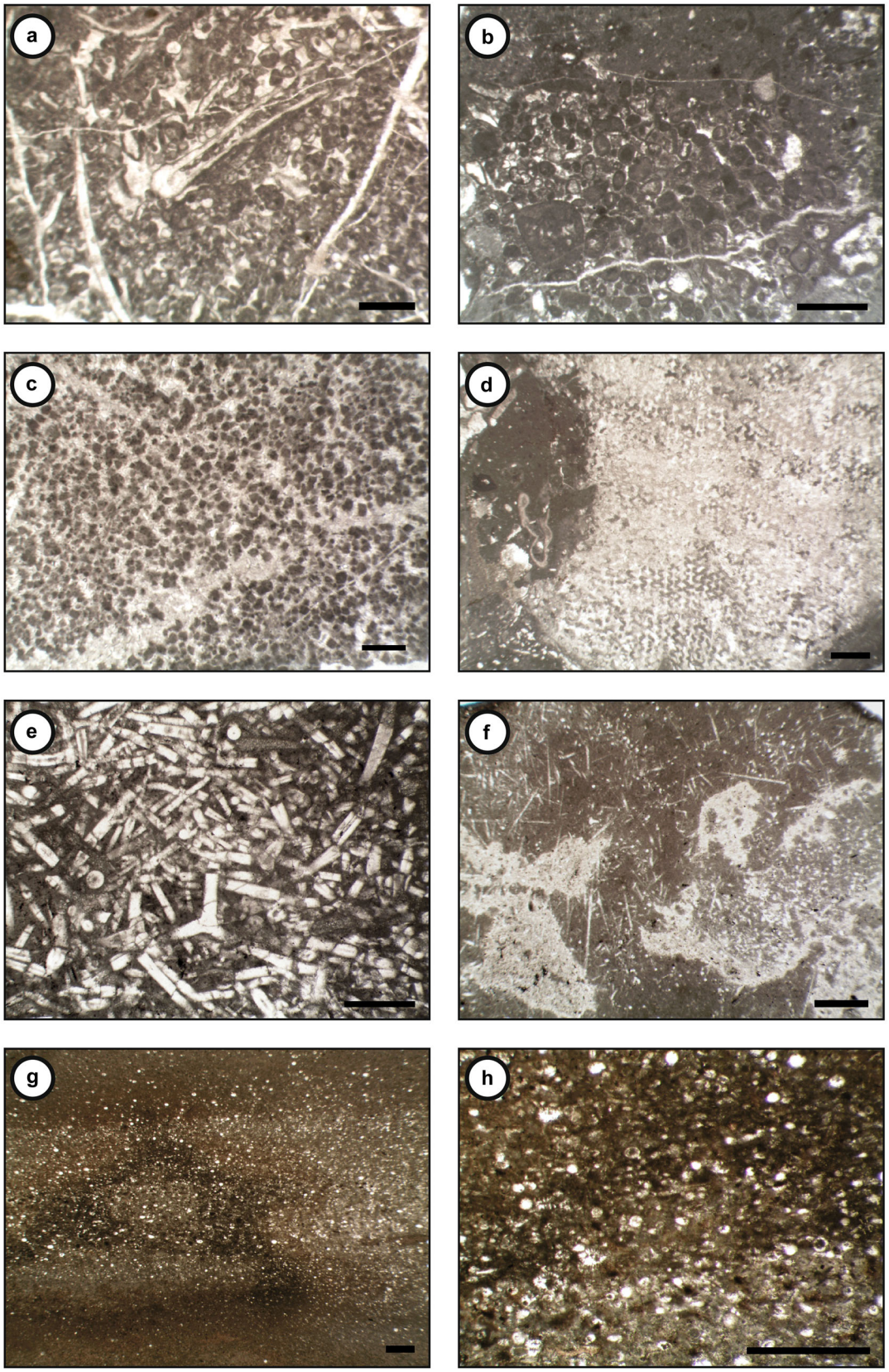

Figure 6. Thin sections images of stones from the mass-flow deposit of event layer E2 (Fig. 5g). (a) Dachstein Formation bioclastic grainstone (lagoonal facies) with dasycladacean algal fragments and a mollusc shell with biogenetic borings in a sparry carbonate matrix. (b). Dachstein Formation grainstone (lagoonal facies) with densely packed, rounded bioclasts with micritic rims ('coated grains') in a muddy carbonate matrix. (c) Dachstein Formation dolomitised limestone with coarse mosaic of dark grey dolomite crystals with syntaxial rims (light grey) and local open vugs (white). (d) Dachstein Formation coral-bearing reef-debris-type carbonate (patch reef facies), containing a coral fragment with radiating septa in a muddy carbonate matrix. (e) Allgäu Formation densely packed spiculite with siliceous sponge spicules (with preserved central canals) in a muddy matrix. (f) Allgäu Formation micritic limestone with thin, calcified sponge spicules and radiolarians with patchy secondary silicification (irregular light grey areas). (g) Ruhpolding Radiolarite Group layered deepwater radiolarite (formerly considered as cherty beds of the Allgäu Formation). (h) Partly preserved shell structure (radial pores) of radiolarians in the layered radiolarite (detail to (g)). Scale bars on the individual images are 1 mm. [Color figure can be viewed at wileyonlinelibrary.com]

This supports the age of 1953 ± 38 CE derived from the AMS ^{14}C-based age–depth model at the same depth. The next, slightly higher ^{137}Cs activity peak (>100 mBq g^{-1}) at 20.0 cm in core segment HAS_2012_D1 (≙19.0 cm MCD) can consequently be attributed to the global maximum of ^{137}Cs fallout that was reached in 1963 CE (Fig. 4c), immediately after the Limited Test Ban Treaty (see Appleby, 2001). This also closely matches the age inferred from the AMS ^{14}C-based age–depth model (1967 ± 35 CE at 19.0 cm MCD). The most prominent ^{137}Cs activity peak (>4000 mBq g^{-1}) at 6.5 cm in core segment HAS_2012_D1 (Fig. 4c; ≙6.5 cm MCD) reflects the fallout from the 1986 CE Chernobyl reactor accident (see Appleby, 2001), also confirming the age derived from the AMS ^{14}C-based age–depth model within dating uncertainty (1998 ± 20 CE at 6.5 cm MCD).

For the dating of the three large-scale event layers, we determined the ages at the respective depths in the (event-free) age–depth model where the event deposits had been removed from the original depth scale of the HAS_2012/2016 master composite sequence (Fig. 4a and 4b). Accordingly, the emplacement of event layers E1, E2 and E3 is dated to 84 ± 48 cal a BP (1866 ± 48 CE), 1058 ± 60 cal a BP (892 ± 60 CE) and 2313 ± 131 cal a BP (363 ± 131 BCE), respectively (Fig. 4b). The comparatively large age uncertainty for event layer E3 is related to the fact that the two nearest AMS ^{14}C dates were obtained 27.0 cm (Poz-87325) and 57.0 cm (Poz-95545) above the top of the event layer, which significantly influences downcore age extrapolation by the Bayesian modelling approach.

Discussion

In general, compositional changes of the Lake Hallstatt sediments not only reflect natural variations of the local environmental conditions, e.g. changes in detrital input by the tributaries that are mirrored by variable thickness and appearance of individual laminae, but to some extent also human impact in the catchment. For example, the abrupt shift from distinctly laminated, organic-rich to faintly laminated, carbonate-rich sediments at 650.5 cm MCD (~1300 CE), which is paralleled by a sedimentation rate increase, most likely reflects the intensification of salt mining activity in the early 14th century CE in response to the quasi-nationalisation of the salt mines by the royal court of Austria in 1311 CE (Barth & Lobisser, 2002; Urstöger, 2009). Forest clearance due to intensified salt mining and associated timber exploitation for mining constructions, firewood and tools during this time supposedly increased the erosion of catchment material and its transport into the lake, most likely causing the observed changes in sediment properties and sedimentation rate. Successively intensified wood use during the 14th and 15th centuries CE with partial deforestation of the high valley and an increase of fire events is confirmed by pollen data from the Siegmoos peat bog (Fig. 1c) (Festi *et al.*, 2021). In contrast, the rather gradual transition towards again more distinctly laminated, organic-rich sediments and lower sedimentation rates above 322.5 cm MCD (~1580 CE) might be related to the establishment of systematic forest management around the mid-16th century CE to ensure continuous provisioning of the salt mines with timber under increasing production (Urstöger, 2009).

In addition to this at least partial impact of human activity on in-lake sediment deposition, the prehistoric mining district itself has repeatedly been affected by geomorphic processes, in particular by large-scale mass movements that left a distinct sedimentological imprint on the landscape. Related deposits have been identified at several positions in the high valley and these events are considered responsible for the destruction of the underground mines at the end of the Bronze Age and during the Iron Age (Rohn *et al.*, 2005; Ehret, 2009a, b). To clarify the relationship between the three large-scale event deposits in the lake sediment record and mass movements that affected the mining district in the high valley, their characteristics, timing, possible trigger mechanisms and potential source areas are evaluated in the following.

Possible trigger mechanisms for the deposition of the large-scale event layers in Lake Hallstatt

Regarding the observed sedimentary structures, event layer E1 as well as the basal part of event layer E2 can be classified as typical mass-flow deposits (see Mulder & Cochonat, 1996). These are generally considered to represent sediment material that either originated directly from the subaquatic slopes or was mobilised from there by material that surged into the lake from the catchment. Plastic deformation and partial disintegration of the sediment during its subaquatic downslope movement is considered responsible for the observed distortion of the layering and intense sediment mixing. In contrast, large-scale turbidites like the one that occurs above the mass-flow deposit in event layer E2 and the one that constitutes event layer E3 are regarded to reflect deposition from turbidity currents (Mulder & Cochonat, 1996) that evolve from subaquatic slope instabilities and downward-travelling mass flows. The distinct tripartition of the E2 turbidite thereby most likely reflects the sequential deposition of sediment that was transported and/or brought into suspension by the subaquatic density flow (Shiki *et al.*, 2000). While the multiple graded sand layers at the base of the E2 turbidite (Fig. 5i) likely reflect several pulses of deposition under high-energy conditions in proximity to the subaquatic mass-flow source (Shiki *et al.*, 2000; Waldmann *et al.*, 2011), the overlying rather homogeneous main part of the turbidite (Fig. 5i) mirrors the gradual settling of fine-grained suspended sediment from the water body (Shiki *et al.*, 2000; Hilbe & Anselmetti, 2014). The terminal clay cap (Fig. 5j) finally represents the finest material, which remained in suspension for a longer time and probably only settled during the mixing period (Sturm & Matter 1978; Waldmann *et al.*, 2011). Together, these mass-flow and turbidite deposits are very similar to deposits that have previously been observed in other lakes and related to large-scale subaquatic mass movements (e.g. Siegenthaler *et al.*, 1987; Monecke *et al.*, 2004; Schnellmann *et al.*, 2006; Lauterbach *et al.*, 2012; Hilbe & Anselmetti, 2014). Nevertheless, there are several mechanisms that can trigger the emplacement of such large-scale mass-flow deposits and/or turbidites in lake basins.

For instance, turbidites can be generated by surface runoff or river flooding after heavy precipitation or snowmelt (e.g. Lauterbach *et al.*, 2012; Swierczynski *et al.*, 2013b; Wirth *et al.*, 2013). Such events can transport large amounts of suspended minerogenic detritus into a lake, causing hyperpycnal flows and consequently the deposition of turbidites (Sturm & Matter, 1978; Mulder & Alexander, 2001). However, while this could explain the formation of the frequent centimetre- to decimetre-scale turbidites in the regular lacustrine sediments of Lake Hallstatt (Fig. 5a), it appears unlikely for the large-scale event layers. This is mainly because the turbidites associated with event layers E2 and E3 are much thicker than typical flood- or surface runoff-generated turbidites (see Swierczynski *et al.*, 2013b; Vannière *et al.*, 2013) and the main tributary Traun River, which is the most likely source of larger amounts of flood-related clastic sediment input, enters the lake distant from the coring sites, making it

unlikely to generate turbidity currents of the dimension necessary to deposit metre-scale turbidites in the deepest part of the lake basin. In addition, event layers E1 and E2 pinch out towards the Traun River delta, which is the opposite of what would be expected for mass movements originating there. As furthermore (1) fluvial input usually only generates turbidites but no subaquatic slope instabilities and large-scale mass-flow deposits as those observed for event layers E1 and E2, and (2) the timing of the emplacement of the three large-scale event deposits does not overlap with prominent regional flood episodes recorded in adjacent Lake Mondsee (see Swierczynski *et al.*, 2013b), it appears very unlikely that river flooding or surface runoff were responsible for the deposition of the three large-scale event layers.

In contrast, mass-flow deposits with overlying co-genetic turbidites can be generated by the spontaneous gravitational collapse of subaquatic slope or delta deposits (e.g. Girardclos *et al.*, 2007; Hilbe & Anselmetti, 2014). However, such a scenario can also most likely be excluded for Lake Hallstatt as the deltas of the tributaries are relatively small (Strasser *et al.*, 2020). It is therefore unlikely that potential spontaneous collapses could have generated mass flows and turbidity currents of a size that would have caused the observed metre-scale mass-flow and turbidite deposits. In addition, the occurrence of large stones and terrestrial plant remains in the E1 and E2 mass-flow deposits argues against a solely subaquatic origin. Furthermore, a spontaneous mobilisation of large sediment volumes from the basin slopes due to overloading appears very unlikely as the entire southern sub-basin of Lake Hallstatt is characterised by >100 m high and >20° steep to nearly vertical slopes (Strasser *et al.*, 2020), offering only very limited space for sediment accumulation.

Another possible trigger of large-scale subaquatic but also subaerial mass movements that propagate under water and finally cause the emplacement of mass-flow deposits and co-genetic turbidites in mountain lakes are earthquakes (e.g. Siegenthaler *et al.*, 1987; Monecke *et al.*, 2004; Schnellmann *et al.*, 2006; Waldmann *et al.*, 2011; Lauterbach *et al.*, 2012; Lauterbach *et al.*, 2019). In general, local earthquake intensities >VI are required to initiate landslides or rockfalls as well as subaquatic mass movements at a respective site (Serva 1994; Inouchi *et al.*, 1996; Monecke *et al.*, 2004; Van Daele *et al.*, 2015). As earthquakes in the Lake Hallstatt area during the last ~100 years did not exceed epicentral intensities (I_0) of IV–V (Lenhardt, 2012), which is actually too small to cause subaerial and subaquatic mass movements, and even the strongest historical earthquakes (I_0 = VIII–X) in Austria and the surrounding countries during the last ~800 years occurred at a considerable distance (>70 km) from Hallstatt (Hammerl & Lenhardt, 1997; Grünthal *et al.*, 2009), earthquakes appear rather unlikely to be the trigger of the large-scale mass movements at first glance. Nevertheless, regional earthquake catalogues are most likely incomplete in the pre-instrumental period, recurrence times of large earthquakes might be much longer than the intervals covered by documentary and instrumental data, and even moderately strong earthquakes (I_0 = VIII–IX) might reach local earthquake intensities >VI and trigger subaquatic mass movements at distances >70 km (Bakun & Wentworth, 1997; Wilhelm *et al.*, 2016). Therefore, particularly when considering the local *hard-on-soft* geology (see Poisel & Preh 2004) and its possible preconditioning by intense and long-lasting precipitation, a seismic triggering of large-scale subaerial and subaquatic mass movements in and around Lake Hallstatt cannot be excluded *a priori*. In general, earthquakes are considered to cause multiple simultaneous subaerial (e.g. rockfalls, landslides) and subaquatic slope failures, which would result in the emplacement of independent but contemporaneous mass-movement deposits at different points of a lake basin (e.g. Schnellmann *et al.*, 2002; Monecke *et al.*, 2004). Although unambiguous evidence for multiple coeval mass movements and thus a seismic trigger of the three large-scale event deposits in Lake Hallstatt is not currently available and could only be provided by high-resolution seismic data of the deeper lake sediment infill, allowing to laterally track the event deposits and identify possibly contemporaneous deposits at other points in the lake basin, we cannot ultimately exclude a seismic trigger of the mass movements that caused the deposition of the three large-scale event layers in the lake.

To summarise, locally confined subaerial mass movements such as rockfalls, landslides or debris flows entering the lake and evolving into subaquatic mass flows (e.g. Schnellmann *et al.*, 2006; Knapp *et al.*, 2018), as well as primarily subaquatic mass movements, both either occurring spontaneously or seismically triggered, are considered the most likely causes for the emplacement of the large-scale event layers in Lake Hallstatt. In this context, a major role of the regional geology for the initiation of spontaneous subaerial mass movements is suggested by the local *hard-on-soft* setting with competent blocks of Hallstatt Formation and Plassen limestones overlying the incompetent salt-bearing rocks of the Haselgebirge Formation and weathered marls of the Allgäu Formation (Rohn *et al.*, 2005; Lotter & Rohn, 2012). Large debris flows that resulted from this particular setting have previously been identified at several positions in the Hallstatt high valley and related sediments have also been found in prehistoric mining cavities (Rohn *et al.*, 2005). Furthermore, large-scale subaerial mass movements in a similar geological setting as in the high valley with rigid limestone slabs overlying a more ductile basement of leached evaporites and weathered marls have also been documented near Bad Goisern, ~9 km north of Hallstatt (Unkel *et al.*, 2013) and near Bad Aussee, ~11 km north-west of Hallstatt (Rohn *et al.*, 2004). However, the initial triggers for such large-scale mass movements remain elusive as they can occur quasi-spontaneously in response to (1) continued leaching of the Haselgebirge Formation (Rohn *et al.*, 2005; Lotter & Rohn, 2012) or (2) long-lasting episodes of precipitation, increasing pore water pressure in the high valley slope deposits (see Anderson & Sitar, 1995), but could also be triggered by earthquakes, as discussed above.

Source, trigger and age of event layer E1

Based on the sedimentological characteristics observed distal to the Hallstatt subaquatic alluvial fan (site HAS_2012-1), event layer E1 can be classified as a typical mass-flow deposit. Although it is very similar to deposits of large-scale mass movements in other lakes, it lacks a large-scale co-genetic turbidite above the mass-flow deposit, which is a frequently described characteristic of such mass-movement deposits (e.g. Siegenthaler *et al.*, 1987; Schnellmann *et al.*, 2006; Lauterbach *et al.*, 2012; Hilbe & Anselmetti, 2014). This likely indicates a relatively proximal position of site HAS_2012-1 to the source area of the initial mass movement, suggesting that it could (1) be related to a failure of the adjacent Hallstatt subaquatic alluvial fan or (2) represent the subaquatic propagation of an initially subaerial mass movement (e.g. landslide, debris flow) that originated in the Hallstatt high valley, moved through the gorge of the Mühlbach (Figs. 1b and 7) and mobilised lacustrine sediments when entering the lake. The latter scenario is corroborated by the presence of a walnut shell (Table 1) and stones in the mass-flow deposit (Fig. 5c), which likely indicate that the mass movement had a primarily onshore origin (see Schnellmann *et al.*, 2006), entered the

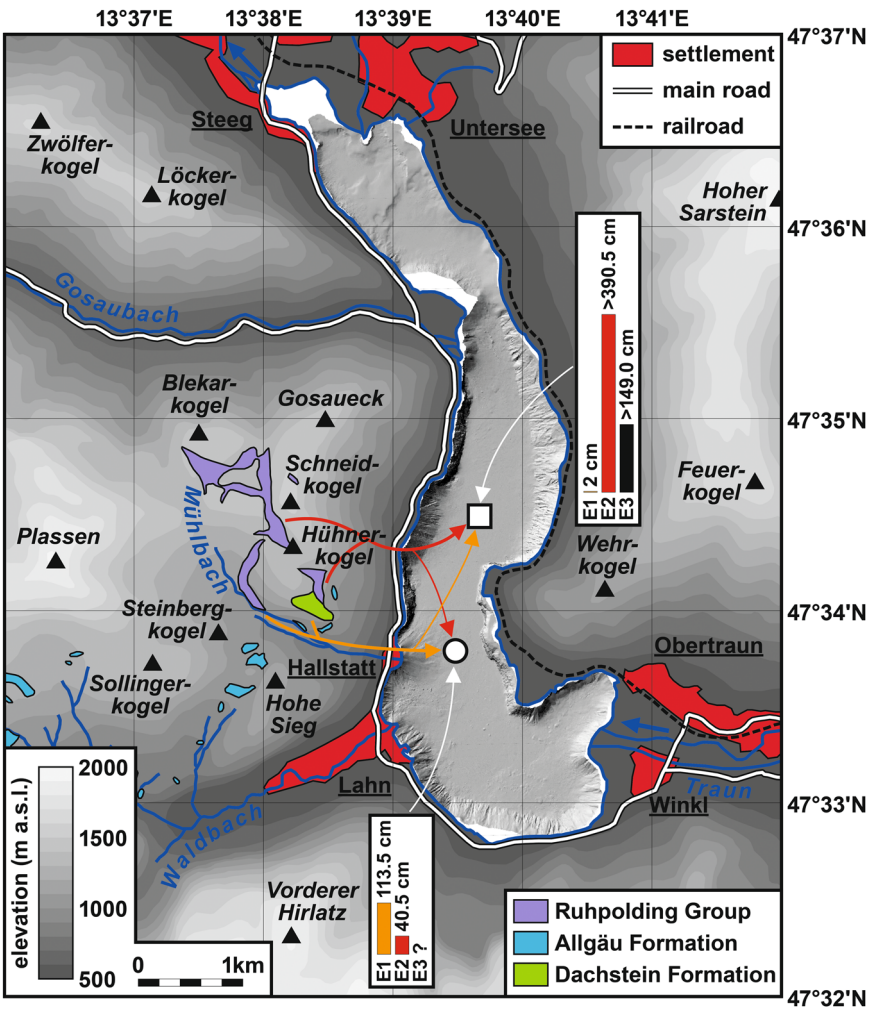

Figure 7. Relief map of the surroundings of Lake Hallstatt and high-resolution multi-beam bathymetry of the lake basin (from Strasser *et al.*, 2020). Coring locations are marked by a white point (HAS_2012-1) and a white square (HAS_2012-2, HAS_2016-1) (for exact coordinates see the main text) and mountain peaks are marked by black triangles. Possible transport pathways for the mass-movement events E1 and E2 are indicated by orange and red arrows, respectively. The thickness of the three event deposits E1 to E3 at the two coring sites is given for comparison. Coloured areas indicate geological units (modified after Schäffer, 1982) from which stones were found in the event layer E2 mass-flow deposit (see the main text and Fig. 6). [Color figure can be viewed at wileyonlinelibrary.com]

lake and thereby mobilised subaquatic slope sediments, and further propagated at the lake floor. However, an earlier deposition of the terrestrial material on the subaquatic alluvial fan and remobilisation by the mass movement that caused event layer E1 cannot be excluded, particularly as the walnut shell is apparently ~250 years older than the emplacement of event layer E1 (Table 1 and Fig. 4). Nevertheless, an origin of the E1 mass movement close to site HAS_2012-1, i.e. at the western lake shore, and its subsequent subaquatic propagation to the east, north and south is supported by the identification of corresponding small-scale turbidites in gravity cores recovered ~200 m east of site HAS_2012-1 (Strasser *et al.*, 2020) and in core segments from the deepest part of the lake basin (e.g. HAS_2016_B1; Fig. 5a), indicating a rapid pinching out of the event layer from its most probable source area (Fig. 7).

A first attempt to date the emplacement of event layer E1 by downcore extrapolation of the information from gamma spectrometry dating on core segment HAS_2012_D1 yielded an age of 1890 ± 8 CE (Strasser *et al.*, 2020). This is in good agreement with the more robust – though slightly less precise – age of 1866 ± 48 CE derived from the ^{14}C-based Bayesian age model, indicating that the event occurred most likely during the second half of the 19th century CE. Based on the initial age estimate, it has been suggested that a local earthquake in 1892 CE with a supposed intensity of I_0 = III–V was responsible for the emplacement of event layer E1 (Strasser *et al.*, 2020). Nevertheless, although there is some, but not unambiguous, evidence from reflection seismic data for a probably synchronous second mass movement south of the Hallstatt subaquatic alluvial fan (Strasser *et al.*, 2020), which would support the idea of multiple coeval subaquatic mass movements and thus a seismic trigger (see. Schnellmann *et al.*, 2002; Monecke *et al.*, 2004), this earthquake was most likely too weak to cause subaerial mass movements and rockfalls as well as subaquatic slope failures (see above). In consequence, and also because of the presence of terrestrial material within the mass-flow deposit, it seems more likely that the emplacement of event layer E1 is related to a massive debris flow after a long-lasting period of precipitation, which did not necessarily cause river flooding but could have increased pore water pressure in the slope deposits in the high valley above a critical threshold and thus caused their failure (see above). This interpretation is in good agreement with local chronicles, which mention large debris flows in 1880 CE and 1884 CE that caused intense damage in Hallstatt as they propagated from the high valley via the Mühlbach gorge directly through the village (Urstöger, 2000).

Source, trigger and age of event layer E2

In contrast to event layer E1, event layer E2 reveals the typical bipartition of large-scale subaquatic mass-movement deposits, i.e. a basal mass-flow deposit and an overlying co-genetic turbidite, previously reported from many deep mountain lakes (e.g. Siegenthaler *et al.*, 1987; Monecke *et al.*, 2004; Schnellmann *et al.*, 2006; Waldmann *et al.*, 2011; Lauterbach *et al.*, 2012; Hilbe & Anselmetti, 2014). Regarding the origin of the initial mass movement that caused the emplacement of event layer E2, a primarily terrestrial origin is indicated by the

presence of stones in the basal mass-flow deposit (see Schnellmann *et al.*, 2006; Fig. 5g), which also allow an assignment of the source area. Besides typical shallow-water carbonate platform rocks of the Dachstein Formation (e.g. lagoonal limestones and dolomitised limestones; Fig. 6a to 6c), which are quite common around Lake Hallstatt (Schäffer, 1982; Mandl *et al.*, 2012) and therefore prevent a precise localisation of the mass movement's source area, coral-bearing reef-debris-type carbonates from the youngest part of the Dachstein Formation (Fig. 6d) as well as limestones and siliceous deepwater sediments from the Allgäu Formation (Fig. 6e to 6f) and the Ruhpolding Radiolarite Group (Fig. 6g to 6h) occur within the mass-flow deposit. As these rocks are only exposed on the mountains along the western lake shore, i.e. at the south-eastern flank of Mt Hühnerkogel and south-west of Mt Gosaueck and Mt Schneidkogel (Fig. 7; Schäffer, 1982; Mandl *et al.*, 2012), their presence within the E2 mass-flow deposit provides strong evidence that the initial mass movement originated from the steep-sloped mountains along the western lake shore and that the material was transported into the lake via the Steingraben gorge (Fig. 7) from where it propagated subaquatically. In contrast, a collapse of the delta of the Gosaubach can be rejected as the cause for the emplacement of event layer E2 because typical rocks from the upper reaches of the Gosaubach, particularly weathering-resistant siliciclastics from the Zwieselalm Formation of the Upper Cretaceous Gosau Group, are missing in the E2 mass-flow deposit. An origin of the mass movement on the western slope of the lake basin, close to site HAS_2016-1, and a subaquatic propagation of the mass flow at the lake bottom towards the south is also suggested by the distinct pinching out of the event deposit between site HAS_2016-1, where it is at least 390.5 cm thick, and site HAS_2012-1, where it only reaches a thickness of 40.5 cm (Figs 2 and 5j). This further implies that the high valley/gorge of the Mühlbach can be rejected as the source area/transport route of the mass movement.

Concerning the trigger of the E2 mass movement, which occurred at 892 ± 60 CE (1058 ± 60 cal a BP), three mechanisms appear reasonable. On the one hand, it could be related to a spontaneous subaerial rockfall, landslide or debris flow, either promoted by the local *hard-on-soft* setting or by long-lasting precipitation (see above). On the other hand, a seismic trigger of the subaerial slope failure also needs to be considered, particularly as there is evidence for multiple coeval subaquatic mass-movement deposits in Lake Achensee in Tyrol (~145 km west) at about the same time (849–1164 cal a BP), which have been attributed to a large remote earthquake (Oswald *et al.*, 2021). A seismic triggering would also be supported by (1) the multiple sand layers at the base of the E2 turbidite, which could be related to several synchronously triggered subaquatic turbidity currents (Van Daele *et al.*, 2017), and (2) the size and geometry of the E2 turbidite, which resembles typical ponded megaturbidites, commonly linked to seiches (e.g. Siegenthaler *et al.*, 1987; Hilbe & Anselmetti, 2014; Van Daele *et al.*, 2015). However, unambiguous evidence for a seismic trigger of event layer E2 is lacking as additional sediment cores and deep-penetrating reflection seismic data from Lake Hallstatt, which could prove the existence of multiple synchronous mass-movement deposits in the lake, are not yet available. Disregarding the ambiguity of the trigger of the initial mass movement, the emplacement of event layer E2 falls within a period for which archaeological evidence for mining activity and possible devastating mass movements in the high valley is so far completely lacking and which is also not covered by local chronicles. Therefore, no further inferences about the possible consequences of this and other, possibly synchronous, mass movements for the local population can be made to date.

Source, trigger and age of event layer E3

In contrast to the large-scale event deposits E1 and E2, no conclusive information about the source area of event layer E3 can be gained from the recovered sediment cores as this event layer is only documented at the base of composite sequence HAS_2016-1, which furthermore only recovered the uppermost part of a large-scale turbidite and neither reached its base nor a possibly underlying mass-flow deposit. This inhibits determination of the potential source area through (1) analysing the provenance of rock material from the mass-flow deposit and (2) examining the direction of motion of the subaquatic mass movement through identification of possibly correlative event layers at site HAS_2012-1, as was done for event layers E1 and E2. Regarding the trigger of the mass movement that caused the emplacement of event deposit E3, which occurred at 363 ± 131 BCE (2313 ± 131 cal a BP), several mechanisms need to be considered. On the one hand, it could again be related to a spontaneous subaerial rockfall, landslide or debris flow, either promoted by the local *hard-on-soft* setting or long-lasting precipitation (see above), and a subsequent subaquatic propagation of the mass movement as proposed for event layer E2. On the other hand, the mass movement could also have been triggered by a larger earthquake. A seismic triggering is corroborated by another series of multiple synchronous mass-movement deposits in the sediment record of Lake Achensee in Tyrol at about the same time (2213–2578 cal a BP), which have also been attributed to a large remote earthquake (Oswald *et al.*, 2021). Such a large earthquake could also have affected the Lake Hallstatt area, causing subaerial as well as subaquatic mass movements, including a possible collapse of the Gosaubach delta, which is characterised by a peculiar shape with an apparently missing eastern part (Fig. 7). However, as there is to date no complementary information regarding possible coeval mass movements from other sediment cores or deep reflection seismics available, the triggering mechanism and source area of mass movement E3 remain elusive.

Although neither the source nor the primary trigger of event layer E3 can be unequivocally determined with the available data, its age interestingly closely matches the end of burial activity on the famous Late Iron Age cemetery in the high valley as well as a reduction in human impact around the mid-4th century BCE (Barth & Lobisser, 2002; Festi *et al.*, 2021). This could suggest that mass movement E3 might be related to a large triggering event that caused multiple coeval mass movements, which possibly also affected the mining district in the high valley. Nevertheless, a direct connection between the emplacement of event layer E3 in the lake and supposed coeval mass movements that possibly caused the abandonment of the cemetery in the high valley is difficult to prove with the available data as the basal mass-flow deposit of event layer E3, which could possibly allow the identification of the source area, has not been recovered.

Conclusions

Based on a suite of sediment cores it was possible to establish a continuous, ~2300-year-long composite sequence of lacustrine deposition in Lake Hallstatt, which is located immediately adjacent to the UNESCO World Heritage-listed Hallstatt underground salt mining district. The most distinct features of this sediment sequence are three large-scale event layers, consisting of mass-flow deposits and/or large-scale turbidites, which are intercalated within the regular (sub-)millimetre- to centimetre-scale laminated lacustrine

background sediments. Their emplacement is dated to 1866 ± 48 CE, 892 ± 60 CE and 363 ± 131 BCE and they are interpreted as representing the deposits of major mass movements. These could either be related to spontaneous or precipitation-triggered subaerial rockfalls, landslides or debris flows in the surrounding steep-sloped mountains but a connection to regional earthquakes has also to be taken into account at least for the older two mass movements. Although it cannot be determined which of these mechanisms was actually causative, the western lake shore was unequivocally identified as the source area for the younger two event layers, whereas a source assignment for the oldest event layer was not possible. Nevertheless, the age of the oldest event closely agrees with a notable reduction of human activity in the Hallstatt high valley during the Iron Age as well as with the abandonment of the famous Late Iron Age cemetery. Although this suggests a connection between mass movements recorded in the lake sediments and similar processes that affected the prehistoric community in the high valley, the comprehensive understanding of the spatio-temporal pattern of past mass movements in and around Lake Hallstatt requires additional research, which is currently under way. This includes deep-penetrating reflection seismics, additional longer and spatially distributed lake sediment cores as well as the detailed geophysical investigation and dating of mass-movement deposits in the high valley. Respective field work has already been finished within the frame of the projects *FaceAlps* and *Hipercorig Hallstatt History (H^3)* and the upcoming results are expected to shed further light on the occupational history of Hallstatt and the impact of natural hazards on the prehistoric mining community.

Acknowledgements. This study was carried out within the framework of a Lise Meitner grant of the Austrian Science Fund (FWF) to S. Lauterbach (grant no. M 1907-N34). The coring campaigns were financially supported by the GFZ German Research Centre for Geosciences. Further financial support was provided by the Austrian Academy of Sciences (ÖAW) through grants to K. Kowarik (project *FaceAlps*) and M. Strasser (project *S^4LIDE*). The work of K. Kowarik and S. Lauterbach was furthermore supported by the *Freunde des Naturhistorischen Museums Wien* and the *Groundcheck* programme of the German Archaeological Institute (DAI), respectively. We thank the municipality and the fire brigade of Hallstatt, the local butchery Zauner and the Österreichische Bundesforste AG for providing administrative and logistic support during the coring campaigns. K. Wendt, S. Barrett, J. Pascual Montañés, B. Brademann, F. Ott, R. Schedel and R. Niederreiter participated in the coring campaigns and contributed significantly to the successful fieldwork. The late G. Schettler carried out the gamma spectrometry measurements, T. Goslar and his team at the Poznań Radiocarbon Laboratory conducted the AMS ^{14}C dating, and J. Moernaut helped with the CT scanning. We thank M. Van Daele and an anonymous reviewer for their constructive reviews and C. N. Roberts for editorial handling. Open Access funding enabled and organized by Projekt DEAL.

Author contributions—**Stefan Lauterbach**: Conceptualization (lead); Data curation (lead); Funding acquisition (lead); Investigation (lead); Project administration (lead); Resources (equal); Software (lead); Supervision (lead); Validation (equal); Visualization (lead); Writing – original draft (lead); Writing – review & editing (equal). **Michael Strasser**: Conceptualization (equal); Funding acquisition (equal); Investigation (equal); Resources (equal); Validation (equal); Visualization (equal); Writing – review & editing (equal). **Kerstin Kowarik**: Conceptualization (equal); Funding acquisition (equal); Investigation (supporting); Project administration (equal); Resources (equal); Visualization (equal); Writing – review & editing (equal). **Hans Reschreiter**: Conceptualization (equal); Investigation (supporting); Project administration (equal); Resources (equal); Writing – review & editing (equal). **Gerhard W. Mandl**: Investigation (equal); Visualization (equal); Writing – review & editing (equal). **Christoph Spötl**: Conceptualization (supporting); Resources (equal); Writing – review & editing (equal). **Birgit Plessen**: Data curation (equal); Formal analysis (equal); Investigation (equal). **Achim Brauer**: Conceptualization (equal); Funding acquisition (equal); Investigation (equal); Resources (equal); Supervision (equal); Writing – review & editing (equal).

References

Anderson SA, Sitar N. 1995. Analysis of rainfall-induced debris flows. *Journal of Geotechnical Engineering* **121**: 544–552.

Appleby PG. 2001. Chronostratigraphic techniques in recent sediments. In *Tracking environmental change using lake sediments. Volume I: Basin analysis, coring and chronological techniques*, Last WM, Smol JP (eds.) Kluwer Academic Publishers: Dordrecht; 171–203.

Bakun WH, Wentworth CM. 1997. Estimating earthquake location and magnitude from seismic intensity data. *Bulletin of the Seismological Society of America* **87**: 1502–1521.

Barth FE. 2013. Die Blockwandbauten des Salzbergtales bei Hallstatt und ihre Verwendung. In *Bronzezeitliche Fleischverarbeitung im Salzbergtal bei Hallstatt*, Pucher E, Barth FE, Seemann R, Brandstätter F (eds.) Austrian Academy of Sciences: Vienna; 93–134.

Barth FE, Lobisser W. 2002. *Das EU-Projekt Archaeolive und das archäologische Erbe von Hallstatt*. Natural History Museum: Vienna; 83.

Beiwl C, Mühlmann H. 2008. *Atlas der natürlichen Seen Österreichs mit einer Fläche ≥ 50 ha. Morphometrie – Typisierung – Trophie*. Bundesamt für Wasserwirtschaft: Vienna; 160.

Bronk Ramsey C. 1995. Radiocarbon calibration and analysis of stratigraphy: the OxCal program. *Radiocarbon* **37**: 425–430.

Bronk Ramsey C. 2008. Deposition models for chronological records. *Quaternary Science Reviews* **27**: 42–60.

Bronk Ramsey C. 2009. Bayesian analysis of radiocarbon dates. *Radiocarbon* **51**: 337–360.

Bronk Ramsey C, Lee S. 2013. Recent and planned developments of the program OxCal. *Radiocarbon* **55**: 720–730.

Ehret D. 2009a. The end of Bronze Age mining. In *Kingdom of Salt: 7000 years of Hallstatt*, Kern A, Kowarik K, Reschreiter H, Rausch AW (eds.) Natural History Museum: Vienna; 66–69.

Ehret D. 2009b. The end of the Hallstatt-era mining. In *Kingdom of Salt: 7000 years of Hallstatt*, Kern A, Kowarik K, Reschreiter H, Rausch AW (eds.) Natural History Museum: Vienna; 158–159.

Faupl P, Wagreich M. 2000. Late Jurassic to Eocene palaeogeography and geodynamic evolution of the Eastern Alps. *Mitteilungen der Österreichischen Geologischen Gesellschaft* **92**: 79–94.

Felber H. 1970. Vienna Radium Institute radiocarbon dates I. *Radiocarbon* **12**: 298–318.

Felber H. 1974. Vienna Radium Institute radiocarbon dates V. *Radiocarbon* **16**: 277–283.

Festi D, Brandner D, Grabner M, Knierzinger W, Reschreiter H, Kowarik K. 2021. 3500 years of environmental sustainability in the large-scale alpine mining district of Hallstatt, Austria. *Journal of Archaeological Science: Reports* **35**: 102670.

Ficker H, Gassner H, Achleitner D, Schabetsberger R. 2011. Ectogenic meromixis of Lake Hallstättersee, Austria induced by waste water intrusions from salt mining. *Water, Air, & Soil Pollution* **218**: 109–120.

Girardclos S, Schmidt OT, Sturm M, Ariztegui D, Pugin A, Anselmetti FS. 2007. The 1996 AD delta collapse and large turbidite in Lake Brienz. *Marine Geology* **241**: 137–154.

Grabner M, Wächter E, Nicolussi K, Bolka M, Sormaz T, Steier P, Wild EM, Barth FE, Kern A, Rudorfer J, Kowarik K, Stöllner T, Reschreiter H. 2021. Prehistoric salt mining in Hallstatt, Austria. New chronologies out of small wooden fragments. *Dendrochronologia* **66**: 125814.

Grünthal G, Wahlström R, Stromeyer D. 2009. The unified catalogue of earthquakes in central, northern, and northwestern Europe

(CENEC) – updated and expanded to the last millennium. *Journal of Seismology* **13**: 517–541.
Hammerl C, Lenhardt W. 1997. *Erdbeben in Österreich*. Leykam: Graz; 191.
Haug GH, Günther D, Peterson LC, Sigman DM, Hughen KA, Aeschlimann B. 2003. Climate and the collapse of Maya civilization. *Science* **299**: 1731–1735.
Hell M. 1952. Die Kleinfunde von der Dammwiese in Hallstatt aus den Jahren 1936–1937. *Archaeologica Austriaca* **11**: 71–88.
Hilbe M, Anselmetti FS. 2014. Signatures of slope failures and river-delta collapses in a perialpine lake (Lake Lucerne, Switzerland). *Sedimentology* **61**: 1883–1907.
Igl R. 2009. Roman remains in Hallstatt. In *Kingdom of Salt: 7000 years of Hallstatt*, Kern A, Kowarik K, Reschreiter H, Rausch AW (eds.) Natural History Museum: Vienna; 176–179.
Inouchi Y, Kinugasa Y, Kumon F, Nakano S, Yasumatsu S, Shiki T. 1996. Turbidites as records of intense palaeoearthquakes in Lake Biwa, Japan. *Sedimentary Geology* **104**: 117–125.
Jarvis A, Reuter HI, Nelson A, Guevara E 2008: Hole-filled seamless SRTM data V4. International Centre for Tropical Agriculture (CIAT). Accessible at: http://srtm.csi.cgiar.org
Kern A. 2009. The archaeology of the cemetery. In *Kingdom of Salt: 7000 years of Hallstatt*, Kern A, Kowarik K, Reschreiter H, Rausch AW (eds.) Natural History Museum: Vienna; 124–135.
Kern A, Kowarik K, Reschreiter H, Rausch AW, Thommes J, Taylor TG. 2009. *Kingdom of Salt: 7000 years of Hallstatt*. Natural History Museum: Vienna; 240.
Knapp S, Gilli A, Anselmetti FS, Krautblatter M, Hajdas I. 2018. Multistage rock-slope failures revealed in lake sediments in a seismically active Alpine region (Lake Oeschinen, Switzerland). *Journal of Geophysical Research: Earth Surface* **123**: 658–677.
Knierzinger W, Festi D, Limbeck A, Horak F, Brunnbauer L, Drollinger S, Wagreich M, Huang J-JS, Strasser M, Knorr K-H, Reschreiter H, Gier S, Kofler W, Herzig C, Kowarik K. 2021. Multi-proxy analyses of a minerotrophic fen to reconstruct prehistoric periods of human activity associated with salt mining in the Hallstatt region (Austria). *Journal of Archaeological Science: Reports* **36**: 102813.
Kowarik K. 2019. *Hallstätter Beziehungsgeschichten. Wirtschaftsstrukturen und Umfeldbeziehungen der bronze- und ältereisenzeitlichen Salzbergbaue von Hallstatt/OÖ*. Studien zur Kulturgeschichte von Oberösterreich 50, Oberösterreichisches Landesmuseum: Linz; 380.
Kowarik K, Reschreiter H. 2009. The earliest traces. In *Kingdom of Salt: 7000 years of Hallstatt*, Kern A, Kowarik K, Reschreiter H, Rausch AW (eds.) Natural History Museum: Vienna; 44–45.
Kremer K, Marillier F, Hilbe M, Simpson G, Dupuy D, Yrro BJF, Rachoud-Schneider A-M, Corboud P, Bellwald B, Wildi W, Girardclos S. 2014. Lake dwellers occupation gap in Lake Geneva (France–Switzerland) possibly explained by an earthquake–mass movement–tsunami event during Early Bronze Age. *Earth and Planetary Science Letters* **385**: 28–39.
Kromer K. 1959. *Das Gräberfeld von Hallstatt*. Sansoni: Florence; 225.
Lauterbach S, Chapron E, Brauer A, Hüls M, Gilli A, Arnaud F, Piccin A, Nomade J, Desmet M, von Grafenstein U, DecLakes Participants. 2012. A sedimentary record of Holocene surface runoff events and earthquake activity from Lake Iseo (Southern Alps, Italy). *The Holocene* **22**: 749–760.
Lauterbach S, Mingram J, Schettler G, Orunbaev S. 2019. Two twentieth-century M_{LH} = 7.5 earthquakes recorded in annually laminated lake sediments from Sary Chelek, western Tian Shan, Kyrgyzstan. *Quaternary Research* **92**: 288–303.
Leitner C, Spötl C. 2017. The Eastern Alps: multistage development of extremely deformed evaporites. In *Permo-Triassic salt provinces of Europe, North Africa and the Atlantic margins – Tectonics and hydrocarbon potential*, Soto JI, Flinch JF, Tari G (eds.) Elsevier: Amsterdam; 467–482.
Lenhardt WA. 2012. Seismotektonik. In *Geologische Karte der Republik Österreich 1:50 000 – Erläuterungen zu Blatt 96 Bad Ischl*, Mandl GW, van Husen D, Lobitzer H (eds.) Geologische Bundesanstalt: Vienna; 104–106.
Lin A, Wang M. 2017. Great earthquakes and the fall of the Sanxingdui and Jinsha civilizations in central China. *Geoarchaeology* **32**: 479–493.
Lotter M, Rohn J. 2012. Geogene Naturgefahren – Ingenieurgeologie. In *Geologische Karte der Republik Österreich 1:50 000 – Erläuterungen zu Blatt 96 Bad Ischl*, Mandl GW, van Husen D, Lobitzer H (eds.) Geologische Bundesanstalt: Vienna; 135–151.
Mandl GW. 2000. The Alpine sector of the Tethyan shelf – Examples of Triassic to Jurassic sedimentation and deformation from the Northern Calcareous Alps. *Mitteilungen der Österreichischen Geologischen Gesellschaft* **92**: 61–77.
Mandl GW, van Husen D, Lobitzer H. 2012. *Geologische Karte der Republik Österreich 1:50 000 – Erläuterungen zu Blatt 96 Bad Ischl*. Geologische Bundesanstalt: Vienna; 223.
McCoy FW, Heiken G. 2000. The Late-Bronze Age explosive eruption of Thera (Santorini), Greece: Regional and local effects. In *Volcanic hazards and disasters in human antiquity*, McCoy FW, Heiken G (eds.) Geological Society of America Special Papers 345, Geological Society of America: Boulder; 43–70.
Monecke K, Anselmetti FS, Becker A, Sturm M, Giardini D. 2004. The record of historic earthquakes in lake sediments of central Switzerland. *Tectonophysics* **394**: 21–40.
Mulder T, Alexander J. 2001. The physical character of subaqueous sedimentary density flows and their deposits. *Sedimentology* **48**: 269–299.
Mulder T, Cochonat P. 1996. Classification of offshore mass movements. *Journal of Sedimentary Research* **66**: 43–57.
Müller J, Schmidt R, Schneider J. 1981. Sedimentologische und pollenanalytische Untersuchungen an drei Kernen aus dem Hallstätter See (Salzkammergut, Österreich). *Anzeiger der Akademie der Wissenschaften in Wien – Mathematisch-Naturwissenschaftliche Klasse* **118**: 73–91.
Oswald P, Moernaut J, Fabbri SC, De Batist M, Hajdas I, Ortner H, Titzler S, Strasser M. 2021. Combined on-fault and off-fault paleoseismic evidence in the postglacial infill of the inner-alpine lake Achensee (Austria, Eastern Alps). *Frontiers in Earth Science* **9**: 670952.
Papadopoulos GA, Gràcia E, Urgeles R, Sallares V, De Martini PM, Pantosti D, González M, Yalciner AC, Mascle J, Sakellariou D, Salamon A, Tinti S, Karastathis V, Fokaefs A, Camerlenghi A, Novikova T, Papageorgiou A. 2014. Historical and pre-historical tsunamis in the Mediterranean and its connected seas: Geological signatures, generation mechanisms and coastal impacts. *Marine Geology* **354**: 81–109.
Poisel R, Preh A. 2004. Rock slope initial failure mechanisms and their mechanical models. *Felsbau* **22**: 40–45.
Preusser F, Reitner JM, Schlüchter C. 2010. Distribution, geometry, age and origin of overdeepened valleys and basins in the Alps and their foreland. *Swiss Journal of Geosciences* **103**: 407–426.
Reimer PJ, Austin WEN, Bard E, Bayliss A, Blackwell PG, Bronk Ramsey C, Butzin M, Cheng H, Edwards RL, Friedrich M, Grootes PM, Guilderson TP, Hajdas I, Heaton TJ, Hogg AG, Hughen KA, Kromer B, Manning SW, Muscheler R, Palmer JG, Pearson C, van der Plicht J, Reimer RW, Richards DA, Scott EM, Southon JR, Turney CSM, Wacker L, Adolphi F, Büntgen U, Capano M, Fahrni SM, Fogtmann-Schulz A, Friedrich R, Köhler P, Kudsk S, Miyake F, Olsen J, Reinig F, Sakamoto M, Sookdeo A, Talamo S. 2020. The IntCal20 northern hemisphere radiocarbon age and calibration curve (0–55 cal kBP). *Radiocarbon* **62**: 725–757.
Reschreiter H, Barth FE. 2005. Neufund einer bronzezeitlichen Holzstiege im Salzbergwerk Hallstatt. *Archäologie Österreichs* **16/2**: 27–32.
Reschreiter H, Kowarik K. 2009. The Dammwiese. In *Kingdom of Salt: 7000 years of Hallstatt*, Kern A, Kowarik K, Reschreiter H, Rausch AW (eds.) Natural History Museum: Vienna; 162–165.
Reschreiter H, Kowarik K. 2019. Bronze Age mining in Hallstatt. A new picture of everyday life in the salt mines and beyond. *Archaeologia Austriaca* **103**: 99–136.
Rohn J, Ehret D, Moser M, Czurda K. 2005. Prehistoric and recent mass movements of the World Cultural Heritage Site Hallstatt, Austria. *Environmental Geology* **47**: 702–714.
Rohn J, Resch M, Schneider H, Fernandez-Steeger TM, Czurda K. 2004. Large-scale lateral spreading and related mass movements in the Northern Calcareous Alps. *Bulletin of Engineering Geology and the Environment* **63**: 71–75.

Rom W, Golser R, Kutschera W, Priller A, Steier P, Wild EM. 1999. AMS ^{14}C dating of equipment from the Iceman and of spruce logs from the prehistoric salt mines of Hallstatt. *Radiocarbon* **41**: 183–197.

Schäffer G. 1982. *Geologische Karte der Republik Österreich 1:50 000 – Blatt 96 Bad Ischl*. Geologische Bundesanstalt: Vienna.

Schnellmann M, Anselmetti FS, Giardini D, Mckenzie JA. 2006. 15,000 Years of mass-movement history in Lake Lucerne: Implications for seismic and tsunami hazards. *Eclogae Geologicae Helvetiae* **99**: 409–428.

Schnellmann M, Anselmetti FS, Giardini D, McKenzie JA, Ward SN. 2002. Prehistoric earthquake history revealed by lacustrine slump deposits. *Geology* **30**: 1131–1134.

Serva L. 1994. Ground effects in intensity scales. *Terra Nova* **6**: 414–416.

Shiki T, Kumon F, Inouchi Y, Kontani Y, Sakamoto T, Tateishi M, Matsubara H, Fukuyama K. 2000. Sedimentary features of the seismoturbidites, Lake Biwa, Japan. *Sedimentary Geology* **135**: 37–50.

Siegenthaler C, Finger W, Kelts K, Wang S. 1987. Earthquake and seiche deposits in Lake Lucerne, Switzerland. *Eclogae Geologicae Helvetiae* **80**: 241–260.

Stadler P. 1999. Aktueller Stand der Absolutdatierung der verschiedenen Gruppen des urgeschichtlichen Bergbaus und eines Blockbaus in Hallstatt aufgrund von 14C-Daten. *Annalen des Naturhistorischen Museums in Wien* **101A**: 69–80.

Strasser M, Berberich T, Fabbri S, Hilbe M, Huang JJS, Lauterbach S, Ortler M, Rechschreiter H, Brauer A, Anselmetti F, Kowarik K. 2020. Geomorphology and event-stratigraphy of recent mass-movement processes in Lake Hallstatt (UNESCO World Heritage Cultural Landscape, Austria). In *Subaqueous mass movements and their consequences: Advances in process understanding, monitoring and hazard assessments*, Georgiopoulou A, Amy LA, Benetti S, Chaytor JD, Clare MA, Gamboa D, Haughton PDW, Moernaut J, Mountjoy JJ (eds.) Geological Society of London: London; 405–426.

Sturm M, Matter A. 1978. Turbidites and varves in Lake Brienz (Switzerland): deposition of clastic detritus by density currents. In *Modern and Ancient Lake Sediments*, Matter A, Tucker ME (eds.) Blackwell: Oxford; 147–168.

Swierczynski T, Lauterbach S, Dulski P, Brauer A. 2013a. Late Neolithic Mondsee Culture in Austria: living on lakes and living with flood risk? *Climate of the Past* **9**: 1601–1612.

Swierczynski T, Lauterbach S, Dulski P, Delgado J, Merz B, Brauer A. 2013b. Mid- to late Holocene flood frequency changes in the northeastern Alps as recorded in varved sediments of Lake Mondsee (Upper Austria). *Quaternary Science Reviews* **80**: 78–90.

Unkel I, Ehret D, Rohn J. 2013. Recurrence analysis of the mass movement activity at Stambach (Austria) based on radiocarbon dating. *Geomorphology* **190**: 103–111.

Urstöger HJ. 2000. *Hallstatt-Chronik. Von den Anfängen bis zum Jahr 2000*. Musealverein Hallstatt: Hallstatt; 746.

Urstöger HJ. 2009. From AD 1311 to the present. In *Kingdom of Salt: 7000 years of Hallstatt*, Kern A, Kowarik K, Reschreiter H, Rausch AW (eds.) Natural History Museum: Vienna; 190–195.

Van Daele M, Meyer I, Moernaut J, De Decker S, Verschuren D, De Batist M. 2017. A revised classification and terminology for stacked and amalgamated turbidites in environments dominated by (hemi) pelagic sedimentation. *Sedimentary Geology* **357**: 72–82.

Van Daele M, Moernaut J, Doom L, Boes E, Fontijn K, Heirman K, Vandoorne W, Hebbeln D, Pino M, Urrutia R, Brümmer R, De Batist M. 2015. A comparison of the sedimentary records of the 1960 and 2010 great Chilean earthquakes in 17 lakes: Implications for quantitative lacustrine palaeoseismology. *Sedimentology* **62**: 1466–1496.

van Husen D. 1979. Verbreitung, Ursachen und Füllung glazial übertiefter Talabschnitte an Beispielen aus den Ostalpen. *Eiszeitalter und Gegenwart* **29**: 9–22.

van Husen D. 1997. LGM and late-glacial fluctuations in the Eastern Alps. *Quaternary International* **38–39**: 109–118.

Vannière B, Magny M, Joannin S, Simonneau A, Wirth SB, Hamann Y, Chapron E, Gilli A, Desmet M, Anselmetti FS. 2013. Orbital changes, variation in solar activity and increased anthropogenic activities: controls on the Holocene flood frequency in the Lake Ledro area, Northern Italy. *Climate of the Past* **9**: 1193–1209.

Waldmann N, Anselmetti FS, Ariztegui D, Austin J, James A, Pirouz M, Moy CM, Dunbar R. 2011. Holocene mass-wasting events in Lago Fagnano, Tierra del Fuego (54°S): implications for paleoseismicity of the Magallanes-Fagnano transform fault. *Basin Research* **23**: 171–190.

Wilhelm B, Nomade J, Crouzet C, Litty C, Sabatier P, Belle S, Rolland Y, Revel M, Courboulex F, Arnaud F, Anselmetti FS. 2016. Quantified sensitivity of small lake sediments to record historic earthquakes: Implications for paleoseismology. *Journal of Geophysical Research: Earth Surface* **121**: 2–16.

Wirobal KH. 1994. *Das Klima von Hallstatt: Besonderheiten, Wetterregeln, Klimageschichte, Naturereignisse*. Musealverein Hallstatt: Hallstatt; 76.

Wirth SB, Glur L, Gilli A, Anselmetti FS. 2013. Holocene flood frequency across the Central Alps – solar forcing and evidence for variations in North Atlantic atmospheric circulation. *Quaternary Science Reviews* **80**: 112–128.